A reliable numerical analysis for large-scale modelling of a high-level radioactive waste repository in the Callovo-Oxfordian claystone

C. Plúa[1,*], M.N. Vu[2], G. Armand[1], J. Rutqvist[3], J. Birkholzer[3], H. Xu[3], R. Guo[4], K.E. Thatcher[5], A.E. Bond[5], W. Wang[6], T. Nagel[6,7], H. Shao[8], O. Kolditz[6,9]

[1] Andra, Meuse/Haute-Marne Underground Research Laboratory, Bure, France

[2] Andra, Châtenay-Malabry, France

[3] Lawrence Berkeley National Laboratory (LBNL), Berkeley, California, U.S.A.

[4] Nuclear Waste Management Organization, Toronto, Canada

[5] Quintessa Ltd, Warrington, UK

[6] Helmholtz-Centre for Environmental Research - UFZ, Leipzig, Germany

[7] Freiberg University of Mining and Technology, Freiberg, Germany

[8] Federal Institute for Geosciences and Natural Resources - BGR, Hanover, Germany

[9] Dresden University of Technology (TUD), Dresden, Germany

[*]Corresponding author: Carlos Plúa (carlos.plua@andra.fr)

Abstract

This paper is devoted to the study of the Thermo-Hydro-Mechanical (THM) responses of a porous rock with low permeability under thermal loading in the context of deep geological disposal of radioactive waste. To this aim, numerical simulations of an illustrative case study of a large-scale high-level radioactive waste (HLW) repository are performed. The considered host formation is the Callovo-Oxfordian claystone, which has been selected for a deep geological disposal facility in France. Within the framework of the DECOVALEX-2019 project, five modelling teams (Andra, LBNL, NWMO, Quintessa, UFZ/BGR) adopted a thermo-poro-elastic approach and proposed different 3D representations of the HLW repository. The differences between teams consisted mostly in the simplification of the geometrical model and the interpretation of the boundary conditions. Numerical results for temperature, pore pressure, and effective stress evolution in the far field, i.e., at the mid-distance of

two HLW cells, were compared between the teams, to quantify the impact of modelling simplifications/assumptions for the assessment of HLW repository. Moreover, plane strain conditions were considered and evaluated in comparison to 3D modelling. Key parameters influencing the THM responses of the HLW repository were assessed by both mono and multi parametric analysis. Spatial variability analysis of THM parameters was also carried out to study the influence of the spatial correlation length on the Terzaghi effective stress and to estimate its probability distribution. The results of these numerical analyses allowed to propose best practice guidelines for modelling large-scale deep geological disposals and deduce the main behavior of the HLW repository.

Keywords: THM coupling; COx claystone; numerical modelling; nuclear waste management.

1. Introduction

The safe and reliable long-term management of the disposal of radioactive waste is a fundamental issue for the environment's protection. A deep geological disposal is the preferred option for radioactive waste storage in several countries. The Callovo-Oxfordian claystone (COx) is being investigated by the French National Agency for Radioactive Waste Management (Andra) to host a deep geological disposal (Cigéo project) for high-level and long-lived intermediate-level waste (HLW and ILW-LL). A scientific and technological research program has been carried out consisting of laboratory tests, in-situ experiments at the Meuse/Haute-Marne Underground Research Laboratory (MHM URL), Thermo-Hydro-Mechanical (THM) model development and numerical modelling. The research program's objectives are to build up knowledge of the geological, hydro-geological, geochemical, structural and mechanical properties of the host rock and its response to disturbance; and to demonstrate the feasibility of constructing and operating of such a facility in the COx formation.[1-3]

In 2005, a 250 km^2 area around the MHM URL, known as the Transposition Zone, was found to have identical geology and properties of the COx matching those observed in the laboratory: the claystone formation has been stable for more than a hundred million years. In 2009, Andra proposed to the French government an underground area of around 25 km^2 inside the Transposition Zone where the underground facility would be built: the Zone of Interest for Detailed Survey (ZIRA). A high-resolution 3D seismic survey of ZIRA provides a detailed description of the vertical and horizontal mineralogical variability of the COx.[4]

The COx formation can be vertically divided into three lithostratigraphic units listed in order from the base (Figure 1)[5]: the Clay unit (UA), approximately two-thirds of total layer thickness with the highest clay mineral content (over 40% on average), the Transition unit (UT), and the Silty Carbonate-Rich unit (USC) with the highest carbonate content (40 to 90%) and a thickness of 20 to 30 m.[3] There is a strong correlation between clay content and porosity values at the level of the COx formation.[6,7] At the main level of the MHM URL, the COx can be considered as a clay matrix (clay content ranging from 40 to 60%) with carbonate and tectosilicate grain inclusions (i.e., non-porous inclusions considered as rigid compared to the clay matrix).[3] As a result, the porosity is located mainly within the clay matrix leading to a very low connectivity for pores larger than 40 nm and low permeability ranging between $1.0 \cdot 10^{-21}$ m^2 and $2.0 \cdot 10^{-20}$ m^2.[8-10]

Mineral distribution maps show a preferential orientation of carbonate and tectosilicate inclusions parallel to the bedding plane.[11] However, the orientation of clay particles and aggregates with respect to the bedding plane is not as marked as in the case of other indurated clays such as the Opalinus Clay in Switzerland. This leads to a comparatively slight anisotropy of most rock properties, particularity in terms of solute diffusion, water permeability, thermal diffusivity and mechanical parameters.

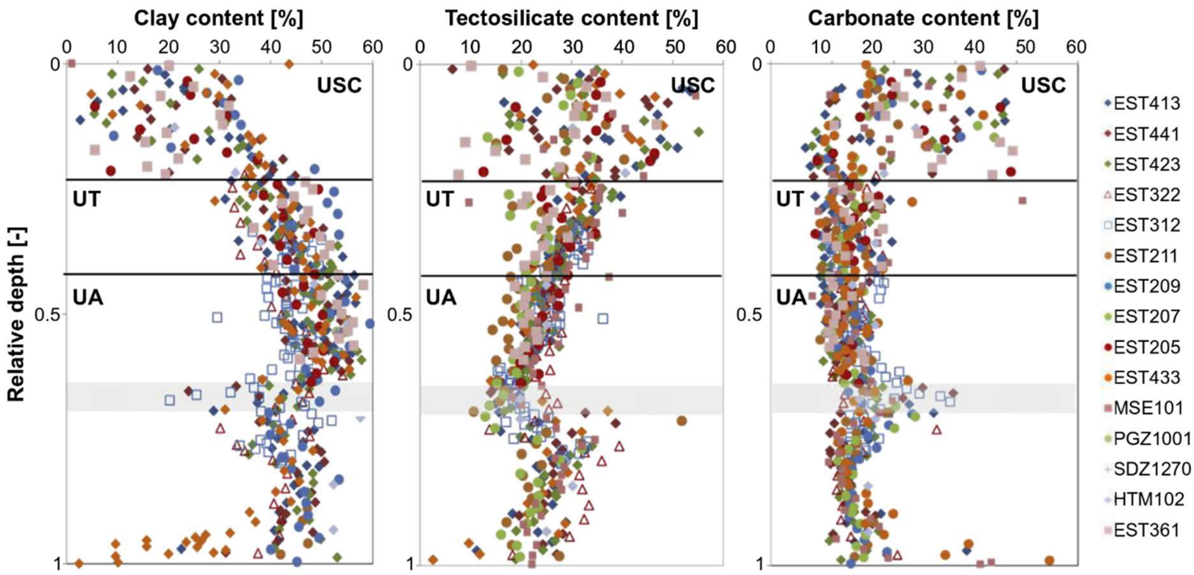

Figure 1 Vertical variations in principal mineralogical phases (clays, tectosilicates and carbonates) of Callovo-Oxfordian obtained in different boreholes around ZIRA (Adapted from Conil et al.[5]).

The current concept for HLW disposal cells in France is based on the emplacement of waste packages in a series of long horizontal micro-tunnels drilled from the access tunnels and favorably aligned with respect to the principal stress field.[3,12-15] The disposal cell design consists of a usable part for package disposal and a head part for cell closure and its length is of order of 150 m for the exothermic HLW and of order of 80 m for the moderately exothermic HLW which will be emplaced in a few cells during a pilot phase.[3,16]

One of the key parameters for the design of the HLW repository is the distance between two parallel cells whose final configuration must fulfill the THM criterion of a maximum temperature of 90 °C in the host rock and no tensile effective stresses in the COx.[3,13,14]

In order to meet these criteria, it is important to understand the THM response of the COx as temperature rises due to the heat emitted by the HLW packages. In a saturated medium with low permeability such as the COx, this thermal loading provokes a pore pressure increase essentially due to the difference between the thermal expansion coefficient of pore water (~$2.3\cdot10^{-4}$ K^{-1} at 20°C and ~$7.2\cdot10^{-4}$ K^{-1} at 90°C) and of solid skeleton (~$1.4\cdot10^{-5}$ K^{-1} for the COx) followed by a slow dissipation of the induced pressure build-up. This thermal pressurization phenomenon has been seen in laboratory tests on undrained samples of the COx.[17,18] Moreover, regarding the HLW repository configuration consisting in parallel cells, lateral compressive stresses are generated at the mid-distance of two parallel cells leading to vertical tensile effective stresses due to the quasi-free expansion of the rock mass in that direction. Numerical modelling of in-situ experiments at the MHM URL has been performed to understand these THM processes.[15,19-22]

Within the framework of the DECOVALEX-2019 project (http://www.decovalex.org; https://decovalex.org/task-e.html), in Task E, five modelling teams with different numerical codes (Table 1) investigated upscaling THM modelling through two in-situ heating experiments at small- and full-scale in terms of cell diameter and an illustrative case study of a large-scale HLW repository.[23] The first part, described in Seyedi et al.,[24] consisted of an interpretative modelling of the small-scale experiment to calibrate the THM parameters through numerical codes and these calibrated parameters were then used for a blind prediction of the full-scale experiment. The modelling teams adopted a thermo-poro-elastic approach and assumed a transversely isotropic behavior of the COx which yielded satisfactory results in terms of temperature and pore pressure. In the second part, described in this paper, the modelling teams studied how to perform reliable numerical modelling at the repository scale (i.e., representative of several parallel cells distributed within several hundreds of meters) by using their numerical approaches developed in the first part. To this aim, different hypotheses were taken into consideration in terms of domain representation and boundary conditions as well as parametric sensitivity analyses and spatial variability analyses were performed. The results obtained from these works are presented as best practice guidelines for modelling large-scale deep geological disposals.

Table 1 Modelling teams and numerical codes.

Acronym of the team	Team	Numerical code
Andra	French National Agency for Radioactive Waste Management	COMSOL[25] and Code_Aster[26]
LBNL	Lawrence Berkeley National Laboratory	TOUGH-FLAC[27,28]

NWMO	Nuclear Waste Management Organisation	COMSOL[25]
Quintessa	Quintessa (funded by Radioactive Waste Management Limited)	COMSOL[25] QPAC[29]
UFZ/BGR	Federal Institute for Geosciences and Natural Resources and Helmholtz Centre for Environmental Research	OpenGeoSys[30-32]

2. Thermo-poro-elastic formulation

In the first part of DECOVALEX-2019 Task E, the two in-situ heating experiments were either numerically interpreted (small-scale experiment) or blind predicted (full-scale experiment) by the modelling teams using the thermo-poro-elastic approach. The description of the water properties was slightly different between teams and the other major difference between teams were found in the interpretation of the boundary conditions. The overall numerical results in terms of temperature and pore pressure were well reproduced with respect to different measuring points.[24] Numerical simulations of in-situ heating experiments in other clayrocks using thermo-poro-elasticity have successfully captured the main THM processes when the host rock is heated (Tamizdoust and Ghasemi-Fare, 2020; Garitte et al., 2017).[33,34] Moreover, the numerical analyses presented in Task E focused on the far field (i.e., beyond the influence of the excavation damaged zone (EDZ) around the HLW cells) where the mechanical effects have a limited influence on the hydraulic behavior. For these reasons, the modelling teams kept their respective numerical codes with no additional modifications with respect to the thermo-poro-elastic formulation used in the first part of Task E.

This section summarizes the governing equations for a classical thermo-poro-elastic saturated medium [35] used by the modelling teams: momentum balance, mass balance, and energy balance. For detailed description of the water properties refer to Seyedi et al.[24]

The momentum balance equation is described as:

$$\nabla \cdot (\boldsymbol{\sigma}' + bp\mathbf{I}) + \rho\mathbf{g} = \mathbf{0} \qquad (1)$$

where $\boldsymbol{\sigma}'$ is the Biot effective stress (negative in compression), b the Biot coefficient, p the pore pressure, $\mathbf{I}$ the identity tensor, $\rho_{eq} = (1-\phi)\rho_s + \phi\rho_w$ the equivalent density of the porous medium with ϕ the porosity, ρ_s and ρ_w the solid skeleton density and water density, respectively, and $\mathbf{g}$ the gravity acceleration vector.

The Biot effective stress $\boldsymbol{\sigma}'$ is expressed by the generalized Hook's law as follows:

$$\boldsymbol{\sigma}' = \mathbf{C}\colon(\boldsymbol{\varepsilon} - \alpha_s(T - T_0)\mathbf{I}) \tag{2}$$

where $\boldsymbol{C}$ is the 4th order elasticity tensor and $\boldsymbol{\varepsilon}$ is the strain tensor, α_s is the linear thermal expansion coefficient of the solid skeleton, T is the temperature and T_0 is the reference temperature.

In addition to the Biot effective stress, the Terzaghi effective stress is used to study the possibility of reaching a critical case (i.e., tensile stress) in the COx layer. The Terzaghi effective stress, $\boldsymbol{\sigma}'^T$, is defined as follows:

$$\boldsymbol{\sigma}'^T = \boldsymbol{\sigma}' + (1 - b)p \tag{3}$$

The water mass balance equation that describes the hydraulic process is given by:

$$\frac{d(\phi\rho_w)}{dt} + \nabla\cdot(\rho_w\mathbf{v}) = 0 \tag{4}$$

with the seepage velocity $\mathbf{v}$ defined by Darcy's law :

$$\mathbf{v} = -\frac{\mathbf{K}}{\mu}(\nabla p - \rho_w\mathbf{g}) \tag{5}$$

where $\boldsymbol{K}$ is the intrinsic permeability tensor and μ is the dynamic viscosity of fluid.

The thermal process is described by the energy balance equation in the following form:

$$(\rho C)_{eff}\frac{dT}{dt} - \nabla\cdot(\boldsymbol{\lambda}\nabla T) + \rho_w C_{p,w}\mathbf{v}\cdot\nabla T = Q \tag{6}$$

where $(\rho C)_{eff} = (1-\phi)\rho_s C_{p,s} + \phi\rho_w C_{p,w}$ is the effective heat capacity with $C_{p,w}$ the specific heat capacity of water, $C_{p,s}$ the specific heat capacity of solid skeleton, $\boldsymbol{\lambda}$ is the effective thermal conductivity tensor of the porous medium, and Q is the heat source.

3. Theoretical case study

A theoretical case representative of a HLW repository is proposed according to the French concept for HLW cells as illustrated in Figure 2.The domain consists in a quarter of the repository assuming two vertical planes of symmetry and is divided into six geological layers: Barrois limestone, Kimmeridgian, Carbonated Oxfordian, Callovo-Oxfordian and Dogger. The COx layer is also subdivided into four units: USC, UT, UA2-UA3 and UA1. For this specific case, the depths of the different geological layers are shown in Table 2.

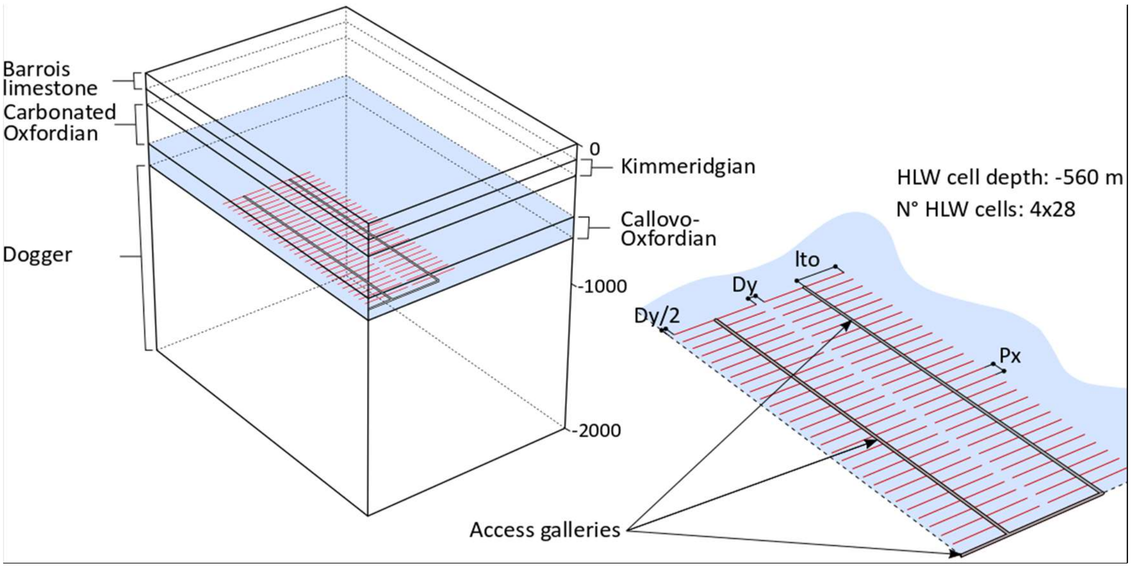

Figure 2 Proposed configuration of a quarter of HLW repository.

The considered HLW repository, located at a depth of 560 m and within the unit UA2-UA3 includes three access galleries, with a diameter of about 10.2 m, two of which lead to one hundred and twelve 150 m long micro-tunnels (diameter = 0.8 m) that are equally distributed at each side. The waste encapsulated in metal canister is placed at the last 142.2 m of the micro-tunnels. The distance between two parallel micro-tunnels is Px = 52.3 m and the distance between the ends of two parallel series of micro-tunnels is Dy = 30.0 m. Note that these two parameters do not reflect the final dimensions planned for the real structure. The teams were free to choose the approach to build the 3D representation of the HLW repository.

Table 2 Depth of the different geological layers.

		Abbreviation	Depth
Barrois limestone		BAR	0.0 m – 103.4 m
Kimmeridgian		KIM	103.4 m – 211.4 m
Carbonated Oxfordian		OXF	211.4 m – 488.0 m
Callovo-Oxfordian	USC	USC	488.0 m - 517.4 m
	UT	UT	517.4 m - 532.6 m
	UA2-UA3	UA23	532.6 m - 595.8 m Cell : 560 m
	UA1	UA1	595.8 m - 635.0 m
Dogger		DOG	> 635.0 m

Four modelling phases were considered. The first phase is the generation of the initial conditions. The second phase starts with the excavation of the access galleries, ten years before the drilling of the micro-tunnels which corresponds to the third phase. The excavation of the galleries and the micro-tunnels are simulated instantly at the beginning of their respective phases. Finally, two years later, the last phase namely the heating phase starts with the HLW package placement inside the micro-tunnels. The results were compared for the last two phases, i.e., year 0 corresponds to the beginning of the HLW cell excavation.

According to the field observations, the initial pore pressure follows a hydrostatic distribution with an additional overpressure in the COx formation that reaches at maximum of 0.5 MPa at the cell depth.

The stress state is geostatic and isotropic for the three upper layers. The anisotropy ratio varies from 1.0 to 1.3 in the Carbonated Oxfordian and, then, it remains constant for the rest of layers as shown in Figure 3. The larger principal stress, σ_H, is parallel to the micro-tunnel axis.

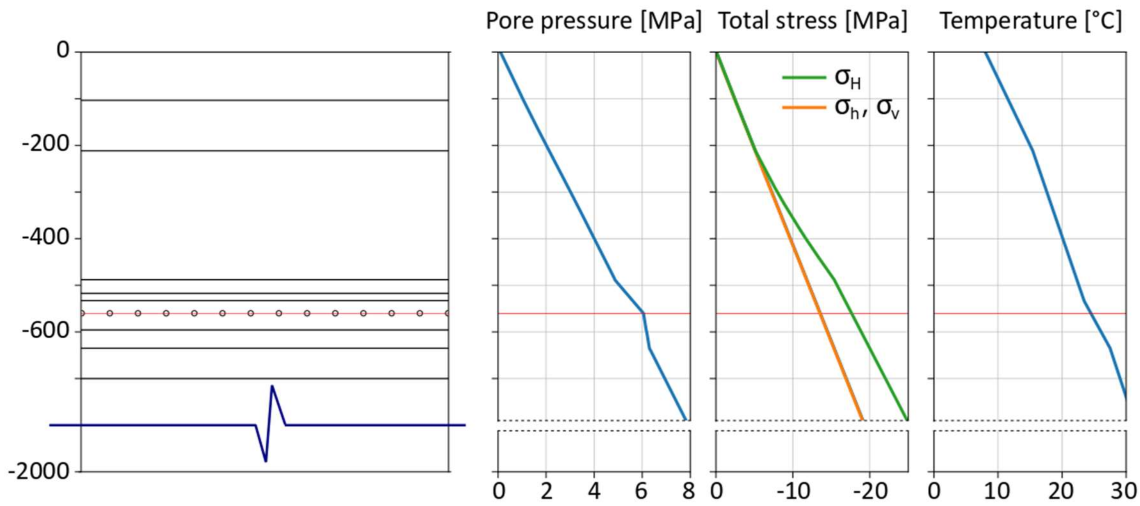

Figure 3 Initial conditions of the HLW repository.

The temperature on the surface was equal to 8.0 ˚C. The geothermal gradients for each layer are given in Table 3 which gives an initial temperature at the cell depth of 24.5 ˚C.

Table 3 Geothermal gradient for each layer [K/m].

BAR	KIM	OXF	USC	UT	UA23	UA1	DOG
0.035	0.035	0.025	0.024	0.024	0.04	0.04	0.024

The boundary conditions were left open to the interpretation of the modelling teams. It was only recommended to impose undrained boundary conditions on the HLW cell walls for the heating phase. The modelling teams were asked to study the influence of different hypothesis regarding the boundary conditions. Table 4 and Table 5 show the boundary conditions that were suggested to the teams in order to make possible a comparison of the numerical results. The atmospheric pressure imposed on the gallery walls was based on that the fully re-saturation after backfilling the galleries take more than

10 000 years. However, the assumption of undrained conditions is also evaluated as a complementary analysis.

Table 4 Boundary conditions on the external surfaces.

	Thermal	Hydraulic	Mechanical
Symmetry boundaries	No heat flux	No fluid flux	Zero normal displacements
Top boundary	Initial temperature	Atmospheric pressure	Free surface
Bottom boundary	Initial temperature	Initial pore pressure	Zero displacements
Access gallery boundary	No heat flux	Atmospheric pressure	Free surface

Table 5 Boundary conditions on the cell wall.

	Thermal	Hydraulic	Mechanical
0-10 years	-	-	-
10-12 years	Initial temperature	Atmospheric pressure	Free surface
12-10000 years	Heat flow (Figure 4)	No fluid flux	Free surface

The head load applied along the last 142.2 m of the micro-tunnels is provided in Figure 4 and is expressed as the average power per unit length of the HLW packages.

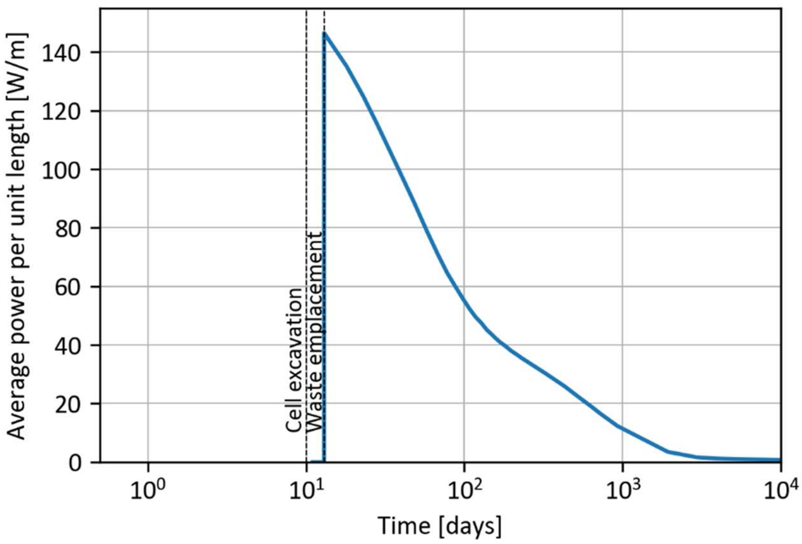

Figure 4 Average power history per unit length of the HLW packages.

Different sets of parameters were provided by Andra in order to carry out a base case (Table 6 and Table 7), parametric analyses (Table 7 and Table 8), and spatial variability analyses (Table 7, Table 8 and Table 9). Table 8 lists the minimum, the mean, and the maximum values that represent the spatial variability of the rock properties within the ZIRA and Table 9 lists their standard deviations. The rock properties follow a normal distribution when the mean and the standard deviation are given, triangular distribution if only the mean is given, otherwise, they follow a uniform distribution.

The numerical results were provided at three different locations. The temperature, the pore pressure as well as the Biot and the Terzaghi effective stresses were studied at the cell depth, in the far field (at the mid-length of two cells), P1, and closer to the cell (at 2.5 cell diameters away from the cell center, i.e., 2.0 m), P2. The vertical displacement was studied at the surface, P3. These points were selected to study the surface uplift and to evaluate the THM indicators: temperature lower than 90 °C and no tensile stresses in the COx.

Table 6 Reference values of the geological layers for the Base Case.

Layer	$\boldsymbol{E_v}$	$\boldsymbol{\nu_{hv}}$	$\boldsymbol{b}$	$\boldsymbol{\phi}$	$\boldsymbol{K_v}$	$\boldsymbol{\rho_{eq}}$	$\boldsymbol{\lambda_v}$	$\boldsymbol{\alpha_s}$	$\boldsymbol{C_p}$
	10^9 Pa	-	-	-	10^{-20} m^2	10^3 kg/m^3	W/m/K	10^{-5} K^{-1}	10^3 J/kg/K
BAR	3.60	0.30	0.60	0.13	10.0	2.45	1.10	2.20	1.024
KIM	3.60	0.30	0.60	0.13	10.0	2.45	1.10	2.20	1.024
OXF	30.00	0.30	0.60	0.13	10000.0	2.47	2.30	0.45	0.925
USC	12.80	0.30	0.60	0.15	1.87	2.48	1.79	1.75	0.978
UT	8.50	0.30	0.60	0.173	1.87	2.45	1.47	1.75	0.978
UA23	7.00	0.30	0.60	0.193	1.87	2.42	1.31	1.75	0.978
UA1	12.5	0.30	0.60	0.164	1.87	2.46	1.63	1.75	0.978
DOG	30.00	0.30	0.60	0.10	100.0	2.47	2.30	0.45	0.925

Table 7 Anisotropy ratio of the geological layers.

Layer	$\boldsymbol{E_h/E_v}$	$\boldsymbol{\nu_h/\nu_v}$	$\boldsymbol{K_h/K_v}$	$\boldsymbol{\lambda_h/\lambda_v}$
BAR	1.00	1.00	1.00	1.40
KIM	1.00	1.00	1.00	1.40
OXF	1.00	1.00	1.00	1.00
USC	1.50	1.00	3.00	1.00
UT	1.50	1.00	3.00	1.50
UA23	1.50	1.00	3.00	1.50
UA1	1.50	1.00	3.00	1.50

DOG	1.00	1.00	1.00	1.00

Table 8 Minimum, mean and maximum of the geological layers.

Layer		E_v	v_{hv}	b	ϕ	K_v	ρ_{eq}	λ_v	α_s	C_p
		10^9 Pa	-	-	-	10^{-20} m^2	10^3 kg/m^3	W/m/K	10^{-5} K^{-1}	10^3 J/kg/K
USC	Min	5.50	0.20	0.60	0.097	2.60	2.42	1.29	1.00	0.842
	Mean	12.80	0.30	-	0.15	1.87	2.48	1.79	-	0.978
	Max	20.1	0.40	1.00	0.185	7.33	2.54	2.45	2.50	1.114
UT	Min	4.00	0.20	0.60	0.143	2.60	2.40	1.08	1.00	0.842
	Mean	8.50	0.30	-	0.173	1.87	2.45	1.47	-	0.978
	Max	12.8	0.40	1.00	0.206	7.33	2.49	1.91	2.50	1.114
UA23	Min	3.70	0.20	0.60	0.15	2.60	2.34	0.98	1.00	0.842
	Mean	7.00	0.30	-	0.193	1.87	2.42	1.31	-	0.978
	Max	10.7	0.40	1.00	0.249	7.33	2.48	1.81	2.50	1.114
UA1	Min	3.80	0.20	0.60	0.128	2.60	2.40	1.12	1.00	0.842
	Mean	12.5	0.30	-	0.164	1.87	2.46	1.63	-	0.978
	Max	21.8	0.40	1.00	0.205	7.33	2.51	2.22	2.50	1.114

Table 9 Standard deviation values of the COx unit layers.

Layer	E_v	v_{hv}	b	ϕ	K_v	ρ_{eq}	λ_v	α_s	C_p
	10^9 Pa	-	-	-	10^{-20} m^2	10^1 kg/m^3	W/m/K	10^{-5} K^{-1}	10^1 J/kg/K
USC	3.70	-	-	2.76	1.83	3.00	0.34	-	6.80
UT	2.70	-	-	1.90	1.83	3.00	0.26	-	6.80
UA23	2.10	-	-	2.90	1.83	4.00	0.25	-	6.80
UA1	5.40	-	-	2.40	1.83	3.00	0.34	-	6.80

4. Modelling approaches

The large number of identical parallel cells led the teams to proposed five different models to represent the domain of the HLW repository. The five approaches were all different, starting with a detailed model containing the 4 × 28 cells and ending with 4 × 1 cells considering symmetry planes. These differences consisted mostly in geometrical simplifications in addition to the differences in the interpretations of the boundary conditions on the far-field boundaries. This allowed to compare different geometrical model approaches and to assess what were the implications of the simplified geometry models with the more complete models in terms of domain representation of the HLW repository.

LBNL proposed the most complete model with domain dimensions of 2.0 km × 1.5 km × 1.0 km and 4 × 28 cells as shown in Figure 5. The minimum element size in the UA23 is 0.8 m for the edge near the cells. At the top and bottom of the domain, boundary elements were applied to consider the constant pore pressure used in the thermal-hydraulic model (with the TOUGH2 simulator), while they were inactive in the geomechanics model (with the FLAC3D code). The access galleries were also explicitly modelled and during the heating phase, the elements were re-activated in FLAC3D.

NWMO presented a similar model with domain dimensions of 2.5 km × 2.0 km × 3.0 km and 6 × 28 cells were considered instead of 4 × 28 cells (Figure 6). However, this model has an important geometrical simplification; all but six cells were considered as panel heating blocks. This hypothesis has been validated in plane strain conditions in Guo et al.[36] The heat power applied in the panel block is the heat power of one cell times the number of simplified cells and the operational length, i.e., 162 × 142.2 m. This simplification allowed to reduce the minimum element size around the cells to 0.62 m.

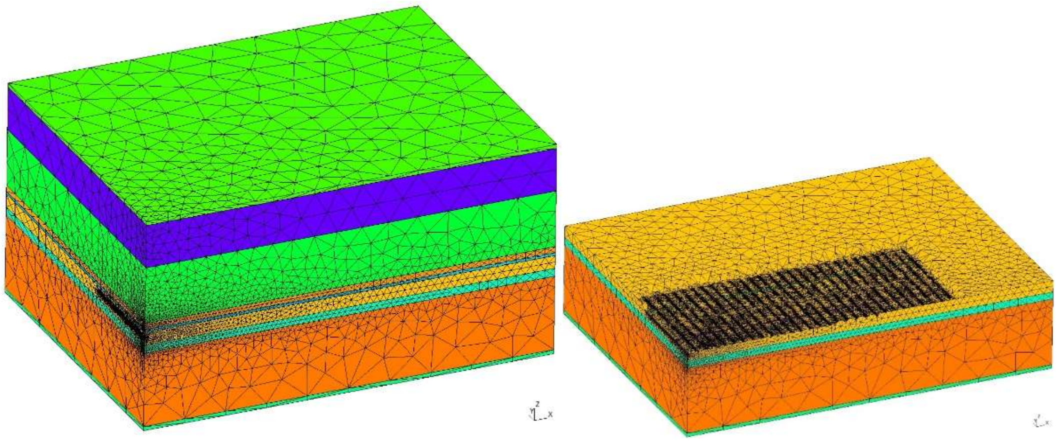

Figure 5 Model geometry proposed by LBNL.

The three other models did not represent the entire quarter of the HLW repository, only a central section of the quarter of the HLW repository was modelled and additional planes of symmetries were assumed.

UFZ/BGR proposed a model with domain dimensions of 523 m X 800 m X 1000 m, with 4 × 10 cells and a minimum element size of 3.9 m (Figure 7). Symmetric boundary conditions were assumed on the four vertical boundaries. Quintessa went further by considering three cells and two half cells on the boundaries as shown in Figure 8. The domain dimensions are 209.2 m X 170.1 m X 1000 m and element sizes in the UA23 range from few cm to 10s of meters. All the vertical boundaries are assumed to be symmetric. Finally, Andra modelled a slice of the quarter of the HLW repository with only 4 × 1 cells (Figure 9). The domain dimensions are 36.15 m X 1500 m X 2000 m and the minimum element size is 0.4 m. This model has three vertical planes of symmetry and one is assumed to be far from the HLW repository. The access galleries were not explicitly modelled by Quintessa so that undrained conditions on their walls were considered. The models of Andra and NWMO assumed drained conditions during the heating phase.

All the modelling teams also worked on simulating the HLW repository in 2D that, basically, consisted in a vertical cross-section of their respective 3D models except for Quintessa that worked with a reduced version of the 3D model as shown in Figure 8.

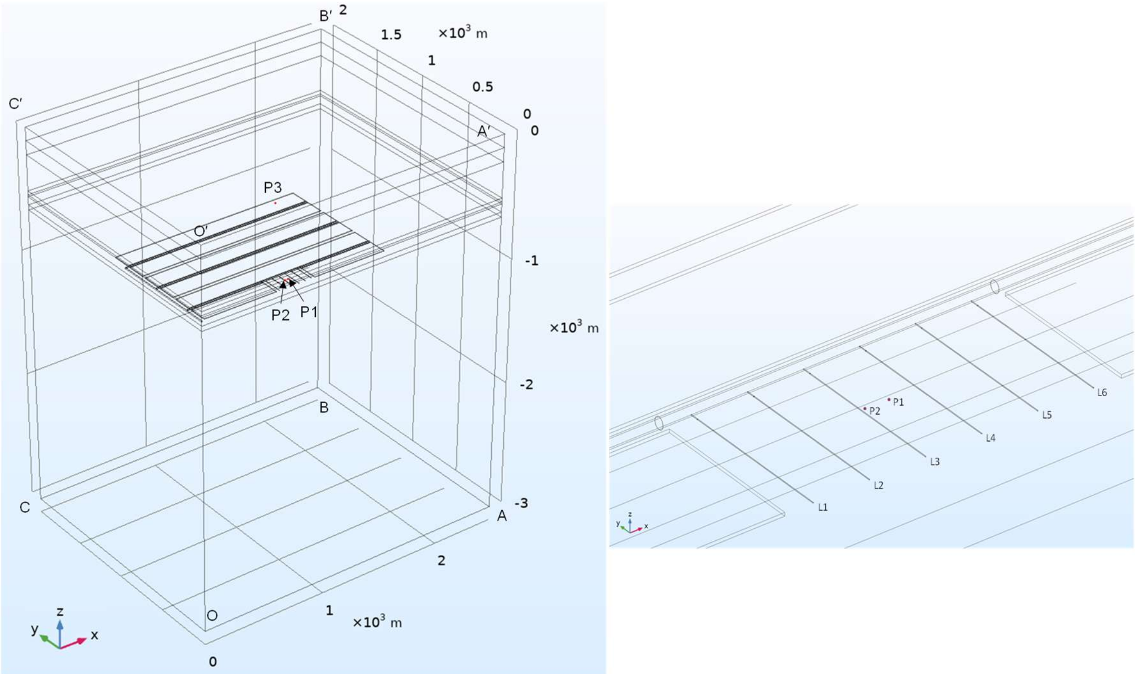

Figure 6 Model geometry with details of 6 placement Cells proposed by NWMO.

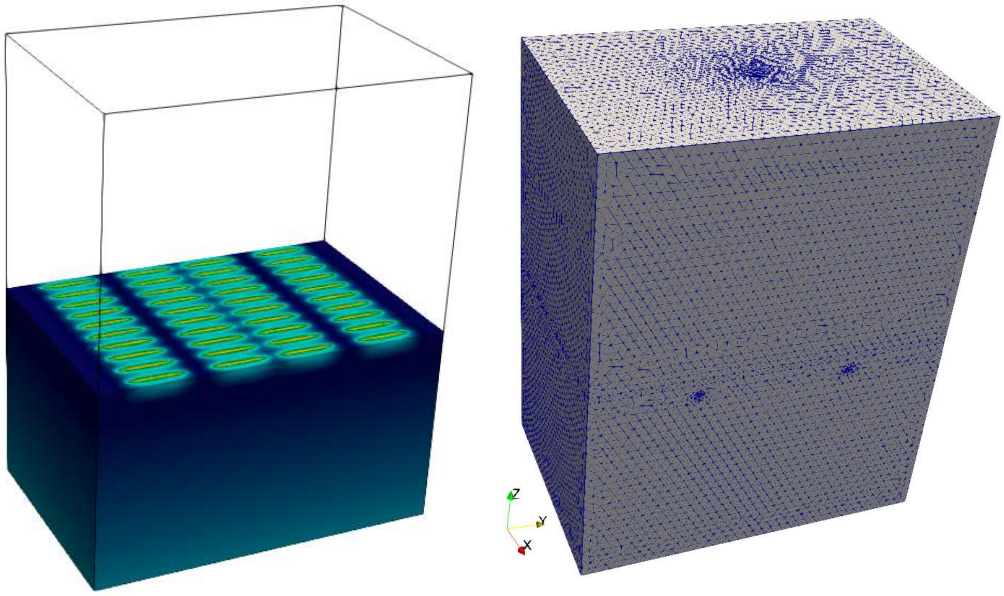

Figure 7 Model geometry and mesh proposed by UFZ/BGR.

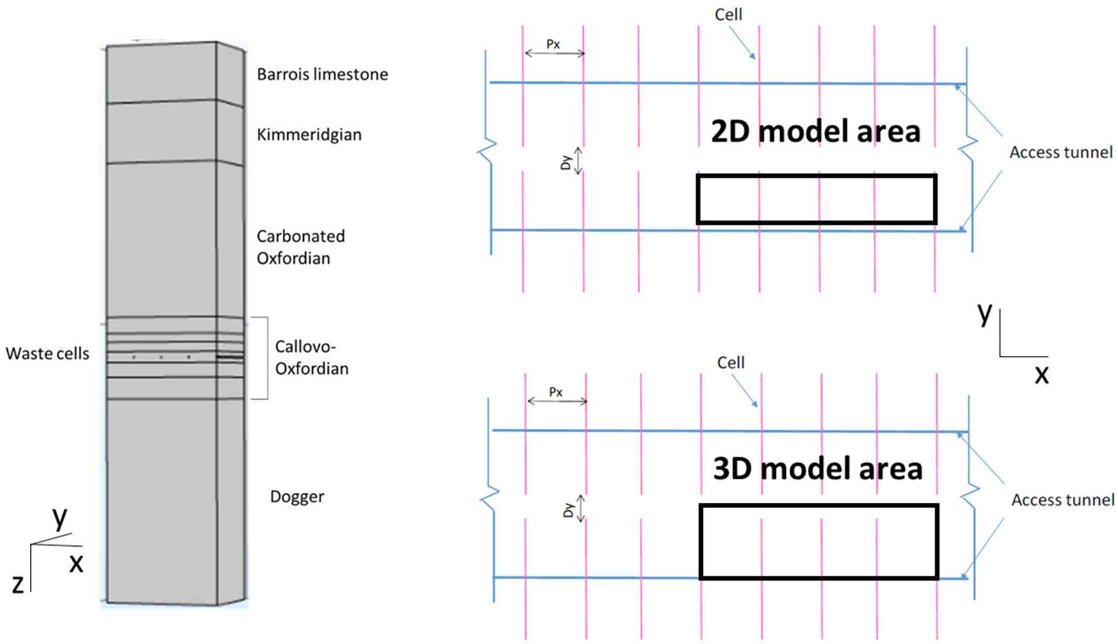

Figure 8 (Left) Model geometry proposed by Quintessa and (Right) horizontal extend of the model domain showing the difference between the 2D and 3D model.

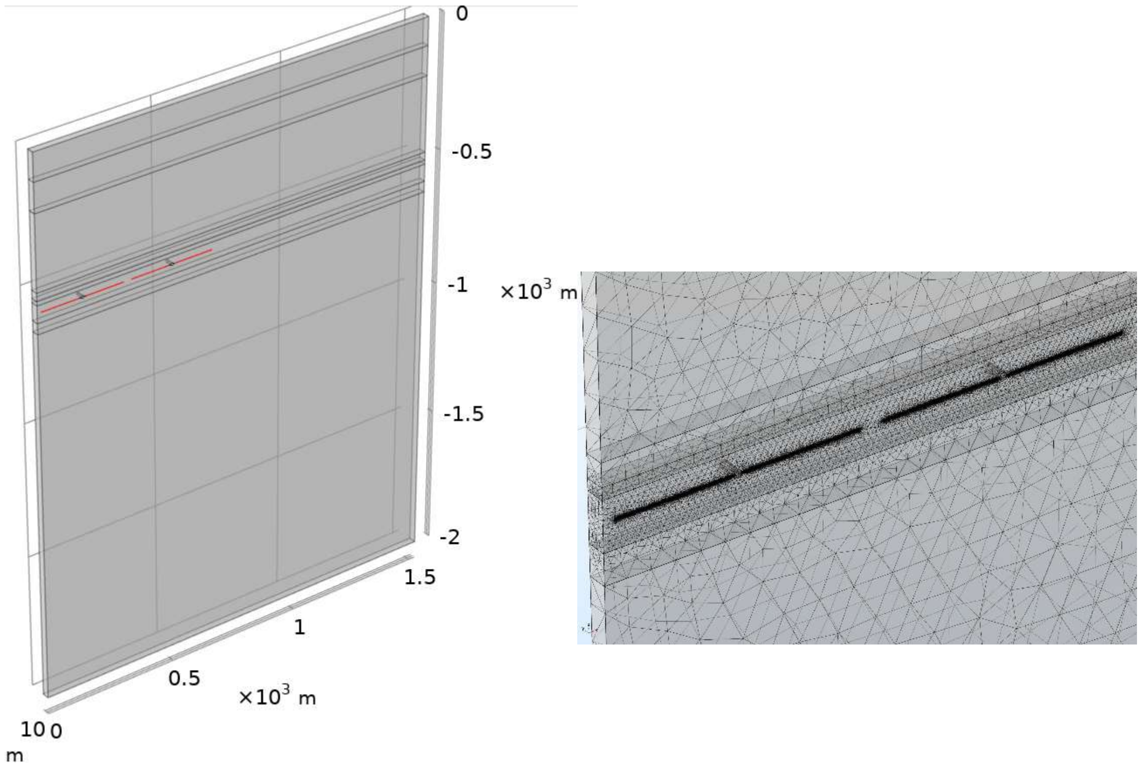

Figure 9 (Left) Model geometry and (Right) mesh proposed by Andra.

In addition to these two studies, the modelling teams worked also on the parametric analysis.

NWMO studied the influence of nine parameters on the THM response of the COx by evaluating their maximum and minimum values (Table 7 and Table 8). It includes three studies:[36] (A) the influence of the minimum or maximum values of each THM parameter used for all layers of USC, UT, UA23 and UA1, (B) the minimum or the maximum values of hydraulic permeability of each layer, (C) the minimum or the maximum values of thermal conductivity for Layer USC, or UA1, or UA23, or UT.

Quintessa also tested the implications of the variation of the nine parameters provided in Table 7 and Table 8. The study consisted of 65 evaluations with different parameterizations and is labeled as study D in the section of results. The four stratigraphic layers were grouped so that the USC, UT and UA1 layers all varied together and the UA23 layer varied separately. Layers were assigned either the mean value, the maximum or the minimum values. These simulations were carried out using the 3D model.

Andra performed a Sobol index analysis in 2D to identify the importance of each parameter in the THM model.[37] Sobol indices determine the contribution of each input parameter and their interactions to the overall model output variance.[38] To this end, SALib Python library (Herman and Usher, 2017) was used to sample and compute the Sobol indices. The sample size is n_{sample} $(2n_{param} + 2)$ where n_{param} is the number of THM parameters and n_{sample} is a baseline sample size which should be large enough to stabilize the estimation of the indices. For these calculations, n_{param} = 9 and n_{sample} = 1000. First and total-order indices were computed; if the total-order indices are substantially larger than the first-order indices, then there are likely higher-order interactions occurring. Two studies were carried out: (E) the contribution of each THM parameter of UA23 unit layer to obtain the maximum values of temperature, pore pressure and Terzaghi effective stress and (F) the contribution of the permeability and the Young's Modulus of the four COx unit layers.

Andra also performed a spatial variability analysis (study G) in 2D to study the influence of the spatial correlation length on the Terzaghi effective stress by using Monte Carlo and to estimate their probability distributions.[37] This analysis was carried out with the help of the Random Finite Element Method (RFEM) software[39] that takes, as inputs, the mean, the standard deviation and the spatial correlation length. For this analysis, only permeability, thermal conductivity, Young's modulus and Biot's coefficient of UA23 with the values listed in Table 7, Table 8 and Table 9 were considered. These last two parameters were inversely correlated. Three horizontal spatial correlation lengths, Θ_x, were tested (20, 10, and 5 m), maintaining a ratio of 1.67 with the vertical spatial correlation length. The number of simulations were 2000 for each case. The maximum and minimum values of the THM parameters were relaxed in order to build the probability distributions that generates the random fields.

5. Model results

5.1 Base Case

The numerical results for the Base Case using the 3D models at points P1, P2 and P3 obtained by the modelling teams are presented in this section.

Figure 10 shows the numerical results of the temperature evolution. The maximum temperature at P1 is 44 °C and occurs 400 years after the waste placement. Near the HLW cells, a rapid temperature increase occurs during the first years achieving a peak of 59 °C, 30 years after the waste emplacement. These temperature values are well below 90 °C. It is worth noting that the models of Andra, NWMO, and Quintessa gave identical results for the first 1000 years. The fact of having a large number of identical parallel micro-tunnel validates the assumptions of symmetry boundary conditions made by Andra and Quintessa considering that the model presented by NWMO represents a complete domain of the HLW repository.

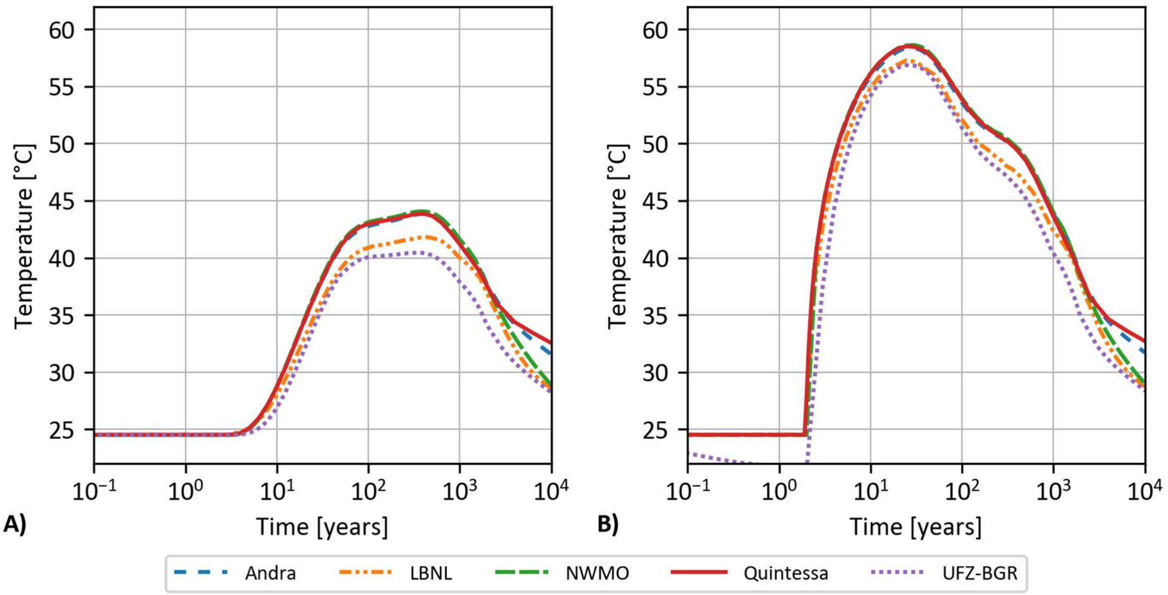

Figure 10 Numerical results of temperature for 3D models at points A) P1 and B) P2.

Figure 11 shows the numerical results of the pore pressure evolution. We observe different maximum values between the modelling teams, although all of them were reached 45 years after the waste placement at the two studied points. The assumption of undrained conditions on the gallery walls implies a lower dissipation after the peak is reached in comparison to the assumption of drained conditions. However, it does not modify the maximum stress, since its effects are noticeable after the peak is reached, as can be seen in Figure 12 that shows the comparison of these two assumptions carried out by NWMO.

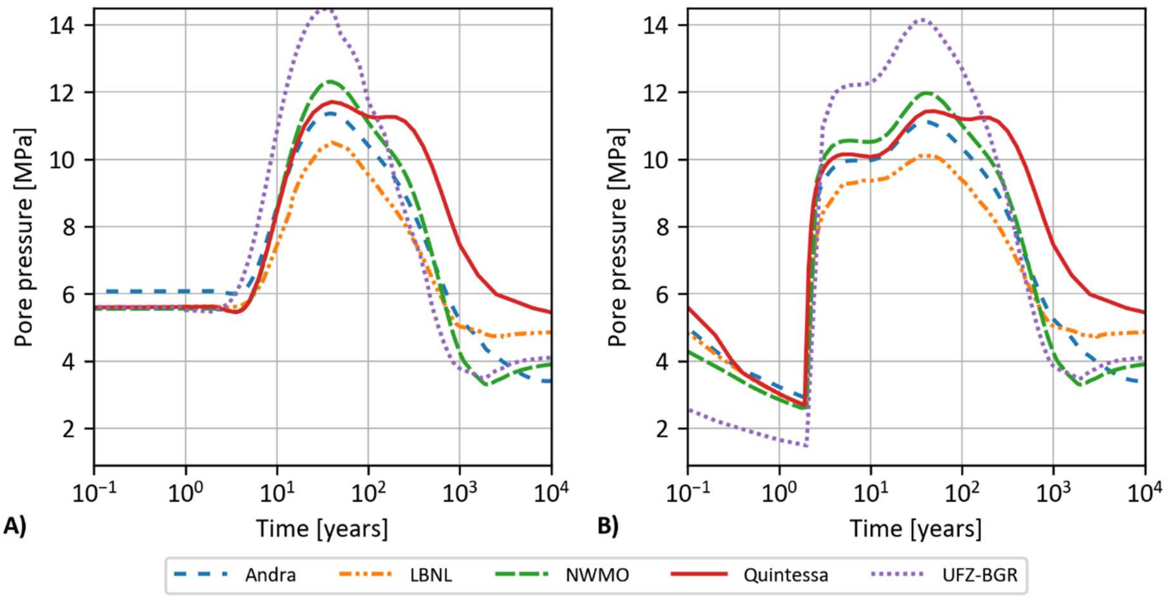

Figure 11 Numerical results of pore pressure for 3D models at points A) P1 and B) P2.

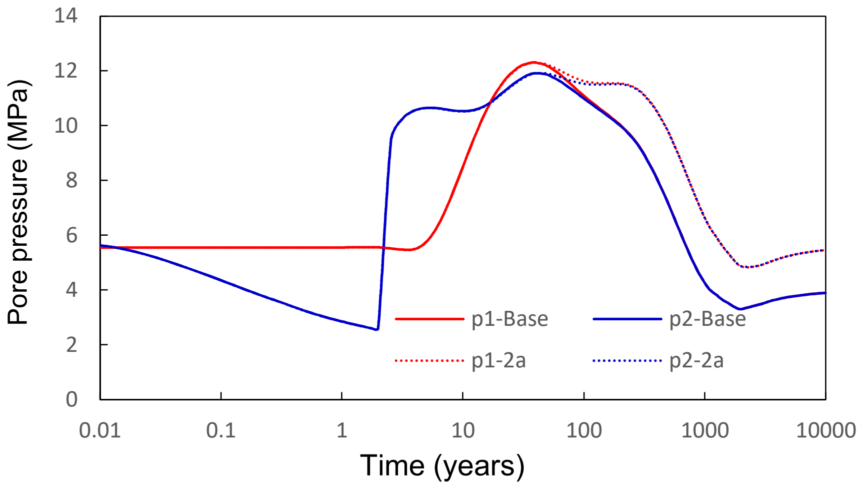

Figure 12 Comparison of pore pressure at points P1 and P2 with two different assumptions on the gallery walls: (Base) drained conditions and (2a) undrained conditions.

Figure 13 shows the vertical Terzaghi effective stress. The maximum values are reached at the same time as the maximum values of pore pressure. The maximum Terzaghi effective stress are lower than -2 MPa which means that no tensile stresses occur during the heating phase. Again, the assumption of undrained conditions on the gallery walls show the most restrictive case at point P1. The maximum Terzaghi effective stress at the far field (point P1) is higher than that at the near field (point P2).

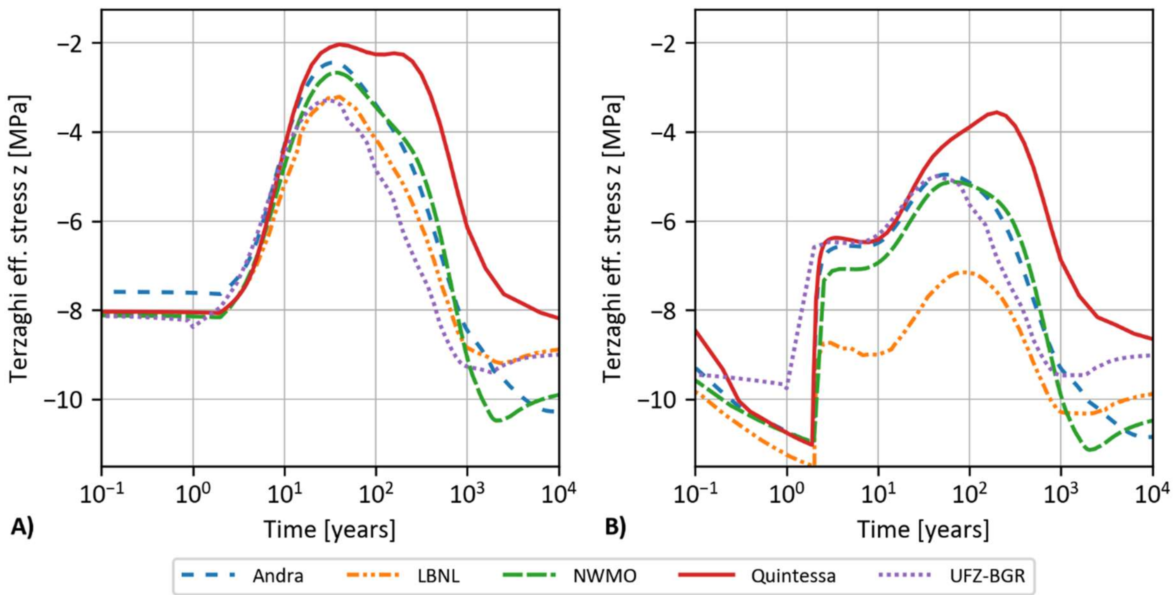

Figure 13 Numerical results of vertical Terzaghi effective stress for 3D models at points A) P1 and B) P2.

The maximum surface uplift occurs 1000 years after the waste placement remains small with values between 7.5 cm and 17.5 cm. Figure 14 shows that the simplified models that contain at least three planes of symmetry tend to induce much larger surface uplift than the more general case of larger 3D repository models. This is due to the lack of lateral expansion possible when an essentially infinite repository is assumed.

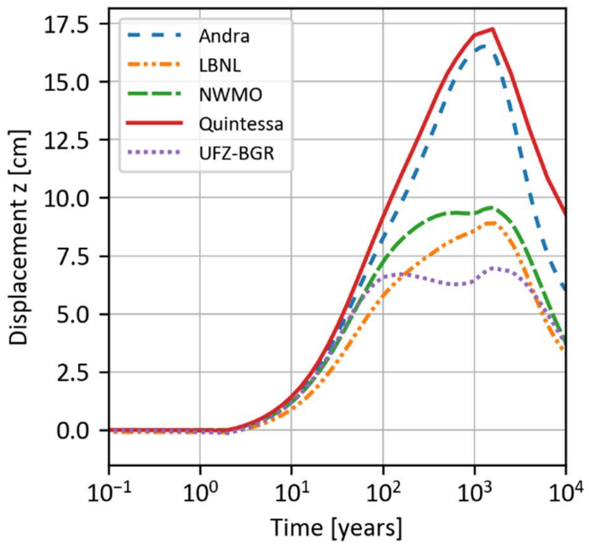

Figure 14 Numerical results of surface uplift for 3D models at point P3.

Furthermore, only the surface uplift was affected by the vertical dimensions of the repository domain. NWMO compares the surface uplift when the model vertical dimensions are 1135 m, 1635 and 2635 m with the uplift from the Base Case which has a vertical dimension of 3000 m as shown in Figure 15. There is no obvious difference in the uplift between the model with a vertical dimension of 2635 m and the Base Case, but, with smaller dimensions (e.g., 1135 m or 1635 m), the uplift is underestimated meaning that the depth of the bottom boundary has some effects on the surface. The numerical results of the temperature, pore pressure and effective stresses did not change.

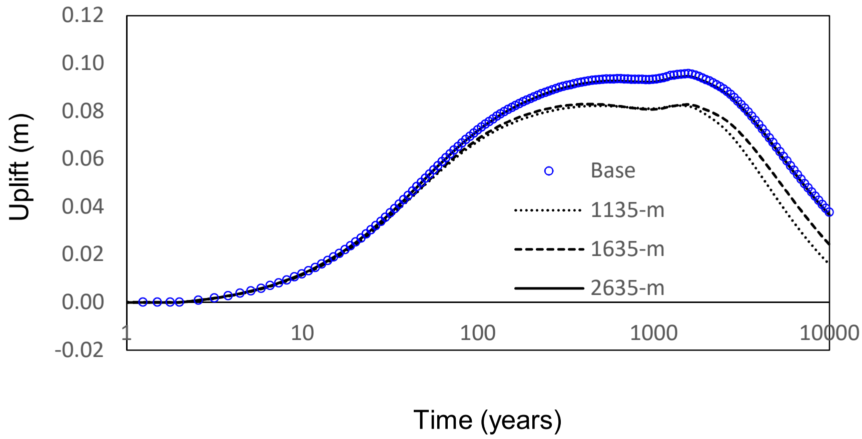

Figure 15 Influence of the vertical dimensions of the repository domain on the surface uplift.

5.2 Plane strain analysis

All the modelling teams performed the same simulation in plane strain conditions with similar results. For visual and illustrative purposes, only the results of NWMO and Quintessa are presented in the following.

In terms of temperature, we observe in Figure 16 that the plane strain assumption implies a negligible change in the near field and about ~3 °C higher in the far field in the temperature maxima with respect to the values obtained in the 3D simulations. The temperature peak of 2D and 3D configuration have same time occurrence.

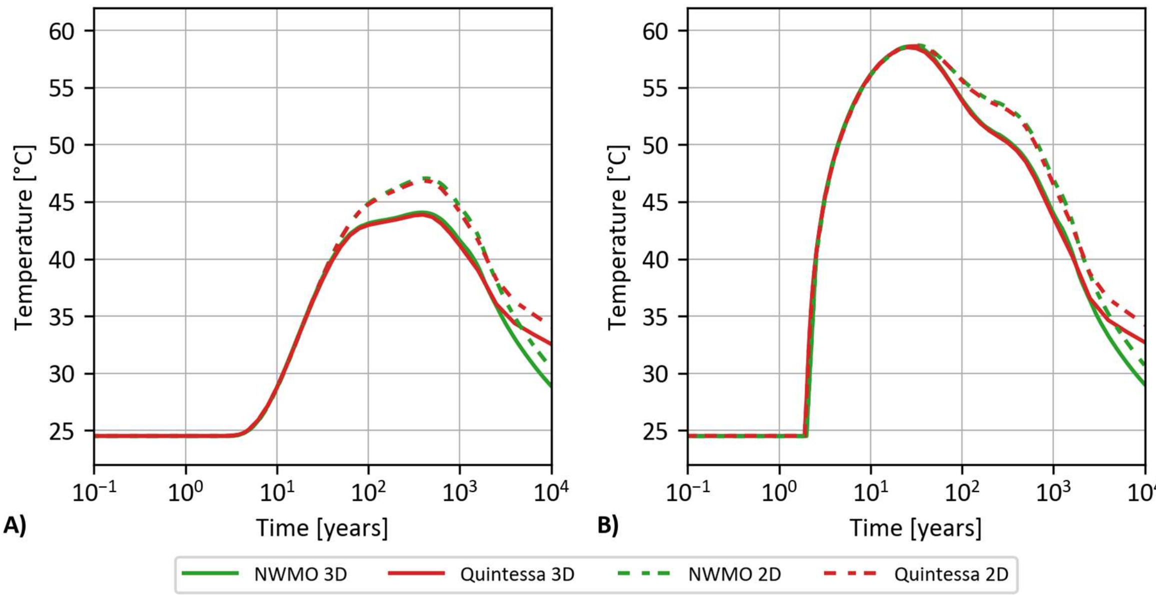

Figure 16 Temperature in 2D and 3D at points A) P1 and B) P2.

On the contrary, the pore pressure shows a different behavior with higher values that tend to dissipate more slowly in plane strain conditions with respect to the results obtained in 3D (Figure 17). Furthermore, the pore pressure peaks are achieved after 100 years of the waste placement. These two aspects are a consequence of having null flux in the longitudinal direction of the cells and can be also seen in the Terzaghi effective stress shown in Figure 18. We observe that the obtained values are still in compression but with values that are closer to a tensile stress state in the far field (point P1).

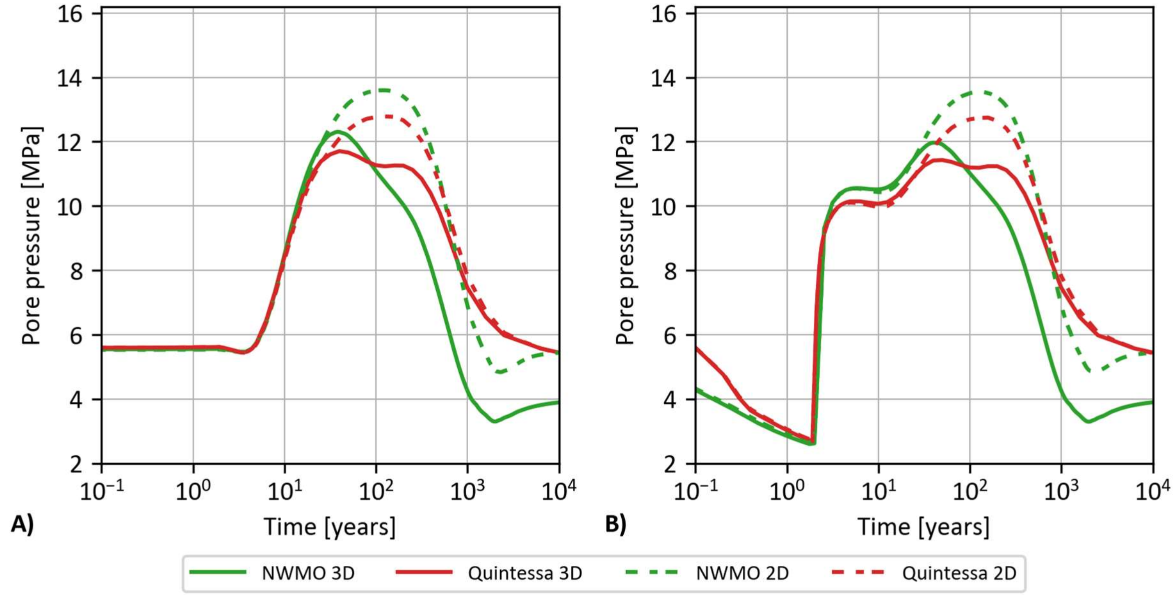

Figure 17 Pore pressure in 2D and 3D at points A) P1 and B) P2.

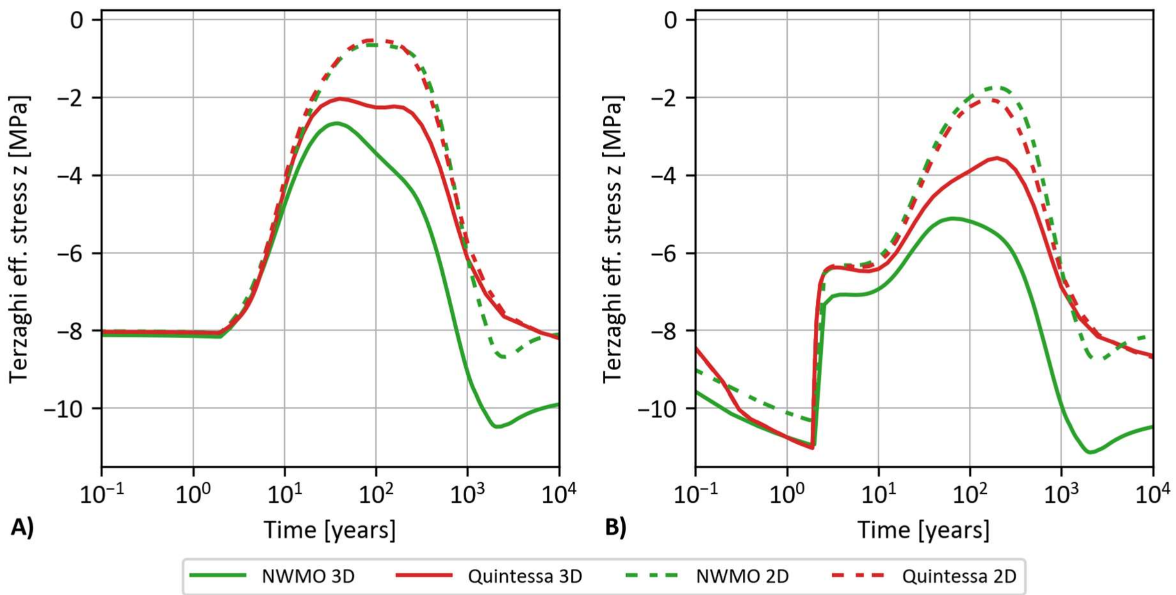

Figure 18 Vertical Terzaghi effective stress in 2D and 3D at points A) P1 and B) P2.

5.3 Geometrical simplifications

NWMO studied how the results may be affected by the use of panel blocks instead of detailed cells since its geometry model was simplified by six panels and only six centered detailed cells. Figure 19and Figure 20 show that reducing to four and two the number of detailed cells has a slight influence on the numerical results of the temperature and the pore pressure, respectively, and regardless the location of the studied points. But increasing the number of detailed cells to eight does not have any change on the results indicating that six detailed cells included in this model are good enough to perform this modelling. Similar conclusions were obtained in terms of the mechanical response. These results validate the assumption of six detailed cells chosen by NWMO which reduces the computational cost of modelling a full HLW repository. This validation exercise was also done under plane-strain conditions by comparing a simplified model with six centered cells and panel blocks against a detailed geometry model.

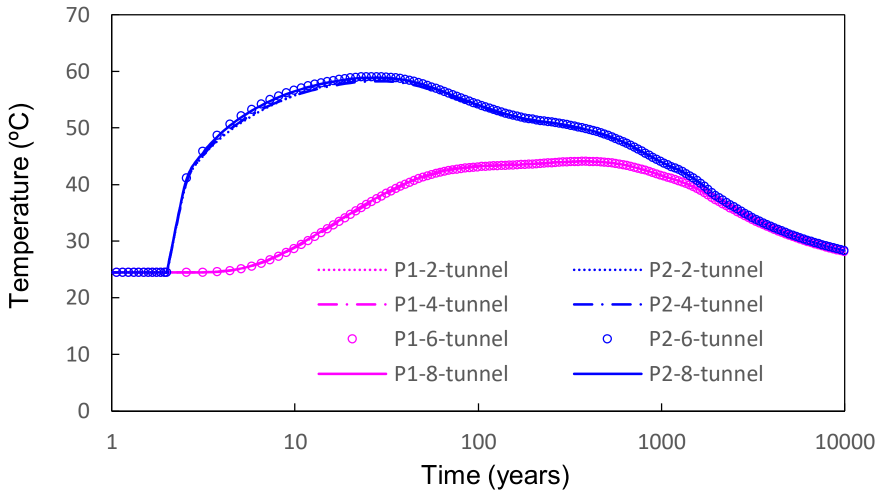

Figure 19 Influence of the number of detailed cells on temperatures at points P1 and P2.

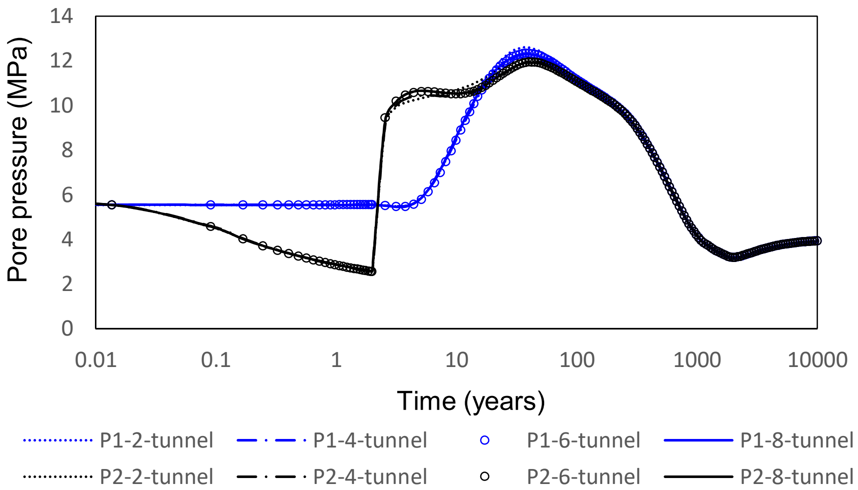

Figure 20 Influence of the number of detailed cells on pore pressures at points P1 and P2.

5.4 Parametric analyses

Figure 21 shows the temperature results carried out in study A. The most important parameter affecting the temperature is the thermal conductivity which produces a difference of 5.2 ˚C between the minimum and the maximum peaks obtained with its maximum and minimum values, respectively.

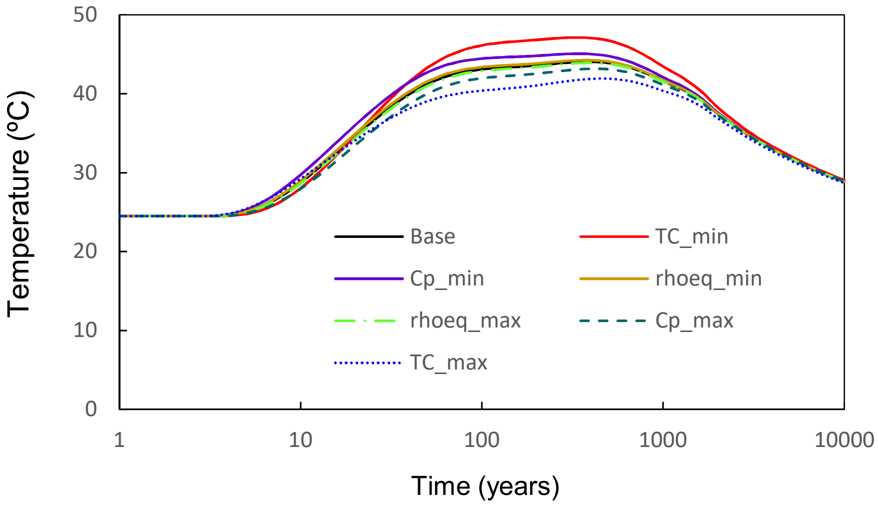

Figure 21 Study A. Temperature at point P1 from base case and cases with maximum or minimum values of thermal conductivity, equivalent density or heat capacity.

Similar conclusions were obtained in study D. Figure 22 shows that the thermal conductivity is the only parameter that affects temperature in the model, with a range in peak temperatures of 7°C. It was confirmed by the results obtained in study E in which the thermal conductivity has the highest Sobol index that contributes to the maximum values of temperature (Figure 23). The similar values of the total- and first-order Sobol indices indicates that there is no interaction between the parameters.

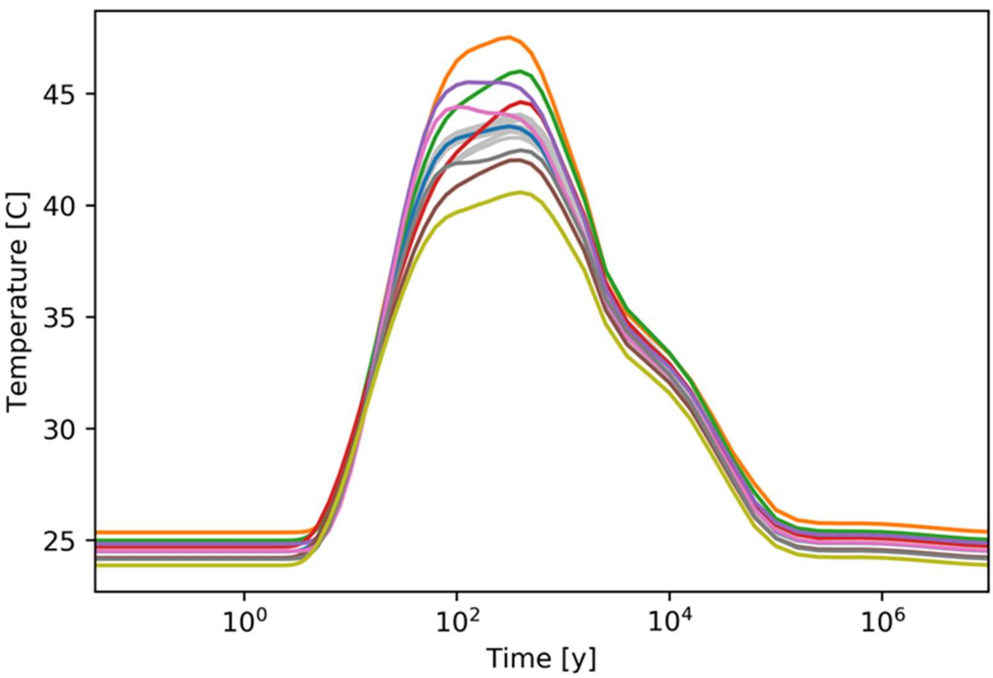

Figure 22 Study D. Temperature at point P1 for 65 parameter sensitivity cases. Cases in which thermal conductivity is altered are coloured, other cases are plotted in grey.

In these studies, the density showed a negligible influence. This can be explained by the small difference between its maximum and minimum values given (Table 8).

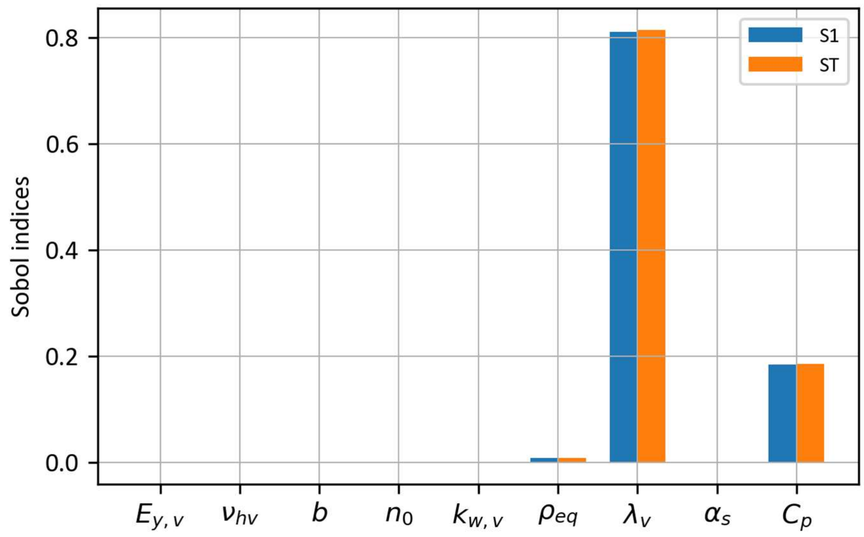

Figure 23 Study E. Sobol indices of the THM parameters contributing to the maximum temperature at point P1.

Regarding the pore pressure, Figure 24 and Figure 25 show the four most important parameters that influence the pore pressure at point P1 according to study D. The permeability shows the highest influence at the maximum and the minimum peak pore pressure. The other three parameters were the Young's modulus, the thermal conductivity and the porosity.

Study A and D reached the same conclusions. Figure 26 shows that the permeability and the Young's modulus have the highest Sobol indices and, as expected, its effects may be magnified if they are changed along with other parameters since their total- and first-order indices are not equal.

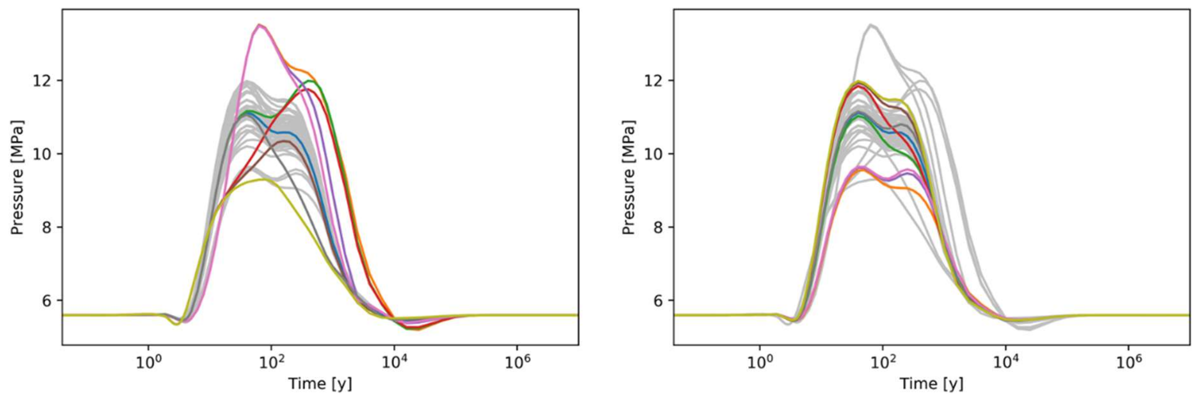

Figure 24 Study D. Pore pressure through time at P1 for 65 parameter sensitivity cases. Cases in which permeability (left) and Young's modulus (right) are altered and coloured, other cases are plotted in grey.

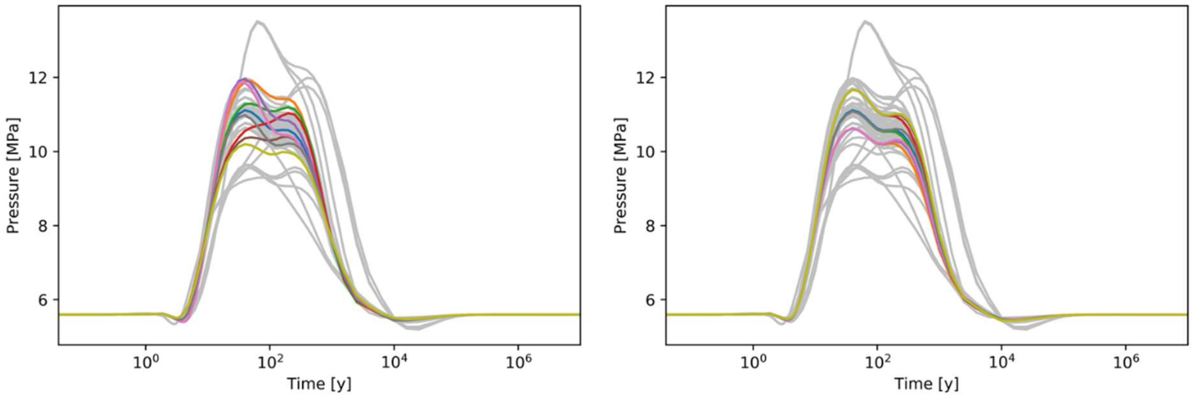

Figure 25 Study D. Pore pressure through time at P1 for 65 parameter sensitivity cases. Cases in which thermal conductivity (left) and porosity (right) are altered and coloured, other cases are plotted in grey.

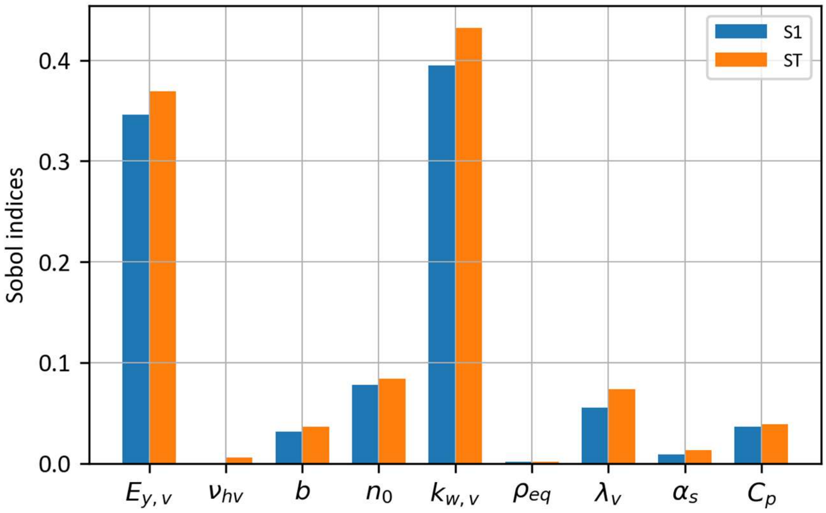

Figure 26 Study E. Sobol indices of the THM parameters contributing to the maximum pore pressure at point P1.

Figure 27 and Figure 28 show the results of the vertical Terzaghi effective stress carried out in the parametric studies D and E. In this case, similar conclusions were drawn although the most important parameter is the permeability in study D and the Young's modulus in study E. Nevertheless, the range of the stress variation under the influence of these two parameters is similar in study D and the same applies to the Sobol indices in study E. Moreover, the parameter variability of the four layers is taken into account in study E whereas only the parameter variability of layer UA23 is studied in study E.

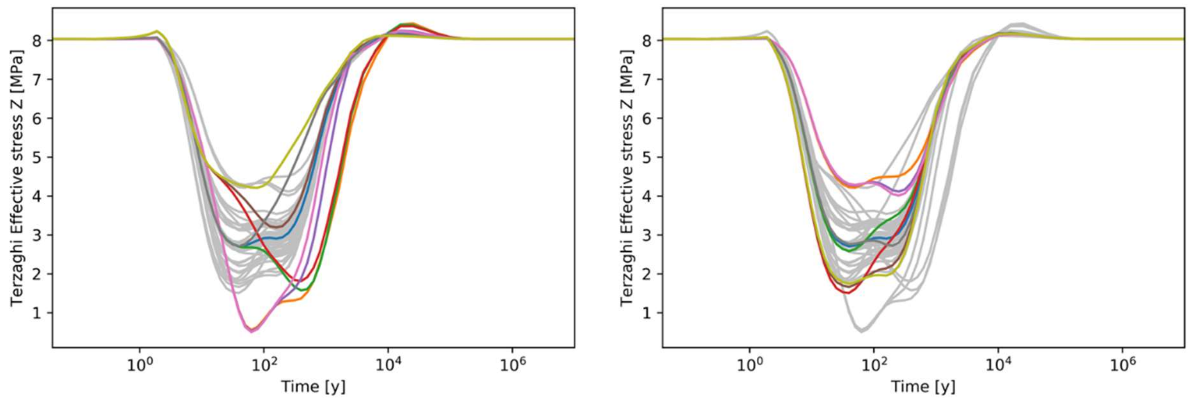

Figure 27 Study D. Vertical Terzaghi effective stress (compressive stress is represented with positive values) through time at P1 for 65 parameter sensitivity cases. Cases in which permeability (left) and Young's modulus (right) are altered and coloured. Other cases are plotted in grey.

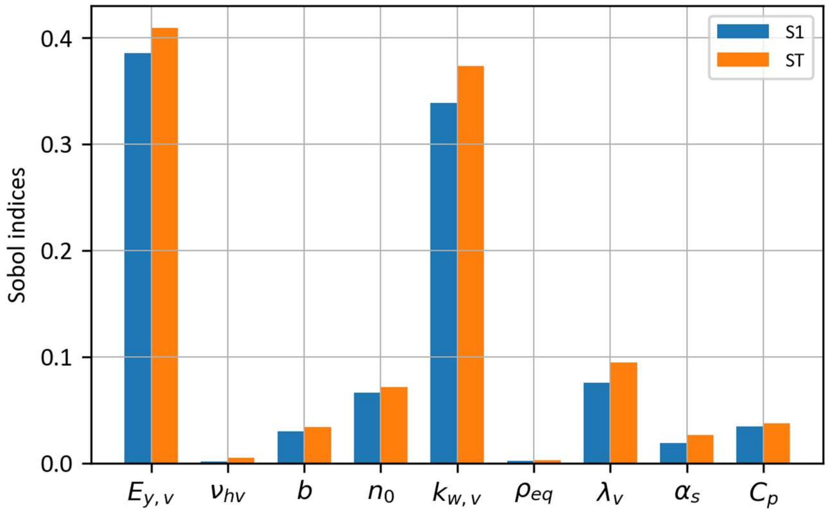

Figure 28 Study E. Sobol indices of the THM parameter contributing to the vertical Terzaghi effective stress at point P1.

Studies B, C and F had, as an objective, the identification of the influence of the parameters surrounding the unit layer UA23 on the temperature, pore pressure and effective stress at point P1. Figure 29 and Figure 30 show that the permeability has no influence on the maximum value of the vertical effective stress and its effects starts to be noticeable after the peak is reached. The same conclusions are drawn from the Sobol analysis as shown in Figure 31 in which the Sobol indices of the permeability and Young's modulus are much higher compared to the other layers' parameters. Figure 32 shows that the thermal conductivity of Layer USC, or UA1, or UT has no influence on the temperature evolution at points P1 and P2.

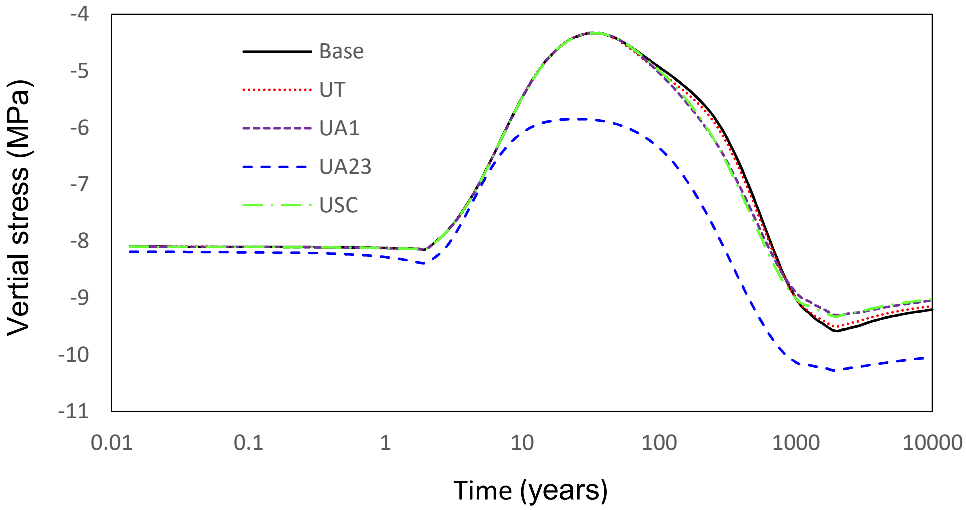

Figure 29 Study B. Influence of maximum permeability values used for layer UT, or UA1, or UA23 or USC on the vertical stress at point P1.

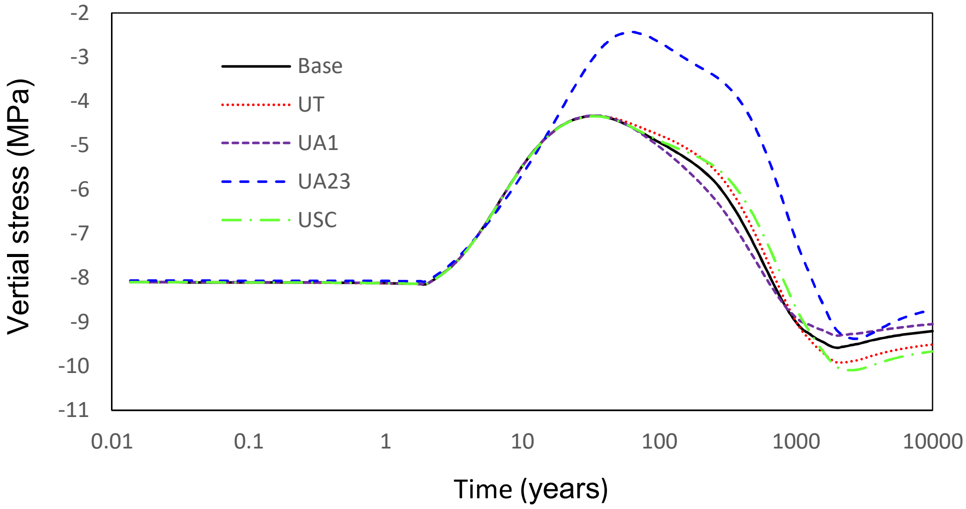

Figure 30 Study B. Influence of minimum permeability values used for layer UT, or UA1, or UA23 or USC on the vertical stress at point P1.

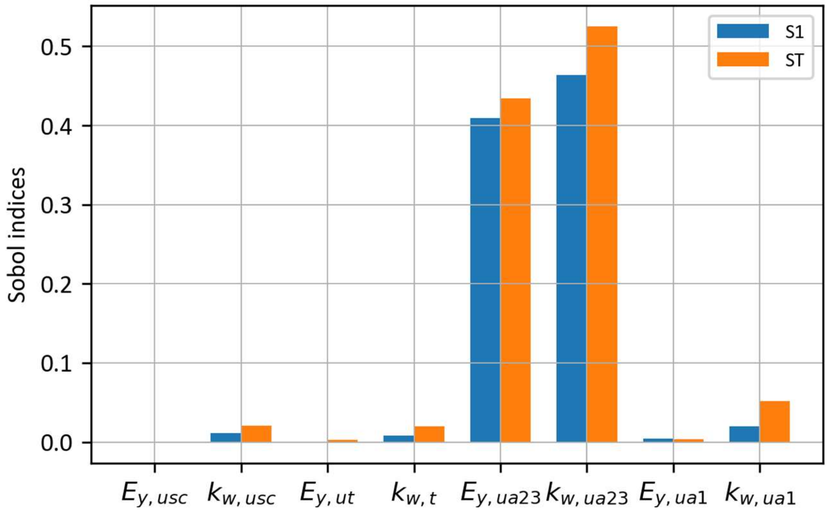

Figure 31 Study F. Sobol indices of the THM parameter of the four unit layers contributing to the vertical Terzaghi effective stress at point P1.

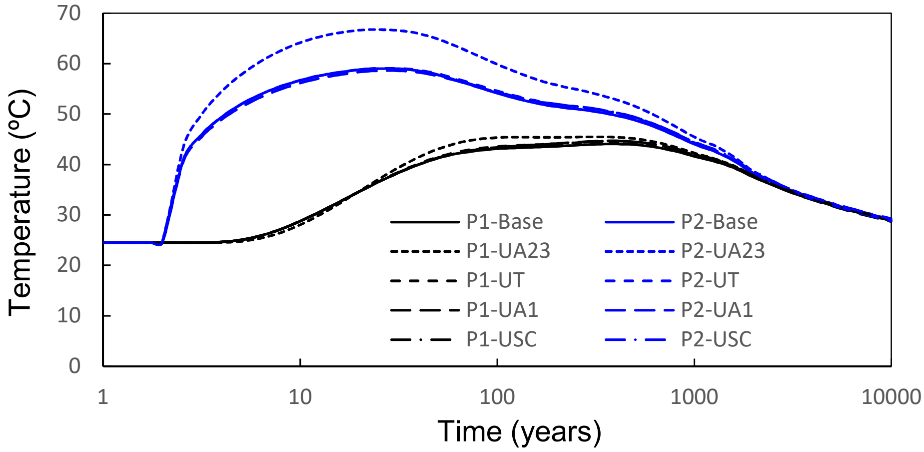

Figure 32 Study C. Influence of minimum thermal conductivity values used of layer USC, or UT, or UA1, or UA23 on temperature at Points P1 and P2.

5.5 Spatial variability analyses

Figure 33 shows the probability and the cumulative distributions of the vertical Terzaghi effective stress at point P1 for the three spatial correlation lengths. The mean is very close to the result obtained for a homogenous layer using the mean values (represented with a black dash line) and the standard deviation is similar in these three cases: 1.11 0.95 and 1.02 MPa. The probability of not having tensile Terzaghi effective stress is 90%. These results show that there is not a strong influence of the spatial correlation length (Table 10).

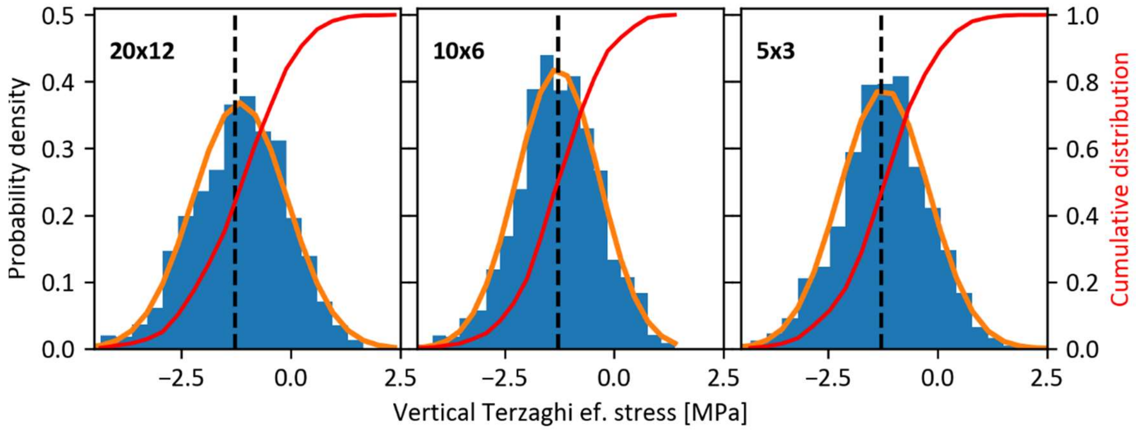

Figure 33 Study G. Probability and cumulative distributions of the vertical Terzaghi effective stress at point P1 for three different length scales: 20 m x 12 m, 10 m x 6 m, and 5 m x 3 m.

Table 10 Mean and standard deviation of the maximum vertical Terzaghi effective stress at Point P1 for three spatial correlation lengths.

		$\mathbf{5 \times 3}$	$\mathbf{10 \times 6}$	$\mathbf{20 \times 12}$
Mean	10^9 Pa	-1.2	-1.3	-1.2
Standard deviation	10^9 Pa	1.0	1.0	1.1

6. Best practice for modelling a large scale HLW repository

Five modelling teams adopted five different approaches and the results of which were compared in order to draw conclusions on the implications of modelling a detailed deep geological disposal. Via such an approach, we can quantify the impact of assumptions or simplifications by evaluating selected THM indicators for the assessment of HLW repositories, such as temperature and effective stress, and other quantities, like pore pressure and surface uplift.

It should be noted that the focus of this step was mainly on the far field (the mid-distance point between two parallel micro-tunnels) and not in the near-field, i.e., EDZ around the HLW cells which was not studied in this work.

Domain geometry

Due to the large number of micro-tunnels, the domain of the HLW repository can be reasonably approximated with few parallel micro-tunnels or even four aligned half micro-tunnels by setting symmetry boundary conditions on their lateral walls. Another interesting approximation can be the simplification of the micro-tunnels as heating panel blocks. This approximation consists in applying the heat power of one cell times the number of simplified cells and the operational length on the panel block.

All these approaches lead to similar results (temperature, pore pressure and effective stress) in the far field with a reduction of computational time with respect to a more detailed representation in which all the micro-tunnels are modelled.

Mesh discretization

The finite element size for the discretization of the domain plays an important role to achieve accuracy in the numerical simulations. Taking into account that the unit layer where the wastes are placed is a few dozens of meters thick, and the diameter of the micro-tunnels was 0.8 m, a range of finite element sizes between 0.4 and 10 m are appropriate to capture well the THM processes at the two evaluated points: two cell diameters away from the HLW cell and the mid-distance between two parallel micro-tunnels. Such element sizes are not accurate enough to represent the processes in the near-field (i.e., EDZ).

Plane strain analysis

Plane strain analysis is an alternative to the 3D modelling of the HLW repositories and could be a preferable option for more time-consuming studies such as parametric analysis or spatial variability analysis. However, it is important to bear in mind that: (a) the results will overestimate the values of certain quantities as compared to a 3D evaluation; for example, ~3°C in temperature and ~2 MPa in vertical Terzaghi effective stress (only in the first few dozens of years are similar values obtained), (b) the maximum values are 50 years later than in the 3D case and (c) these maximum values of pore pressure and effective stress are achieved after a smooth increase after which they tend to decrease much more slowly rather than sharp peaks as observed in the 3D simulations. This is because these simplified geometries essentially assume an infinite extent for the HLW repository.

Boundary conditions

The assumption of undrained conditions on the gallery walls change the behavior of the hydro-mechanical response at the mid-distance between two parallel micro-tunnels and the numerical results show the same effects that are obtained in plane-strain conditions. It is worth mentioning that these changes are observed after the maximum values are reached. Thus, the peaks and their times of occurrence are not influenced by the assumption of undrained conditions on the gallery walls.

The depth of the domain can be fixed to 500 m below the HLW cell level. Setting the bottom boundary at this distance proved to be large enough to obtain accurate results of temperature, pore pressure and effective stress, and only the surface uplift is slightly affected reaching the maximum values 1000 years after the emplacement of the HLW packages.

Parametric analysis

Having an importance ranking of all THM parameter and their interactions is helpful for interpreting conceptual models, as well as for deciding in which subset of parameters put more effort when calibrating such models. The parametric analysis performed for the case study showed that the thermal conductivity was the most important parameter affecting the maximum values of temperature whereas the permeability and Young's modulus were the most influential parameters affecting the pore pressure and the effective stress. Furthermore, the effects in the neighboring formations were not considerable, only the permeability of the surrounding unit layers showed to have a slight influence on the pore pressure and the effective stress.

A complete parametric analysis requires also to identify the interactions between parameters, a feature that is expected to be significant in coupled THM models.

Spatial variability analysis

Spatial variability presented of the rock properties may affect the maximum values of the THM indicators as well as their respective locations with respect to the results obtained under the assumption of homogeneous rock properties. Performing a spatial variability analysis helps to quantify these differences as well as to study the influence of the spatial correlation length. In the case study using the thermo-poro-elastic approach, the means of maximum vertical Terzaghi effective stress obtained from the analyses were similar to the one obtained with mean THM parameters and there was a negligible influence of the spatial correlation length on the Terzaghi effective stress in the range of values that were tested: 20 m × 12 m, 10 m × 6 m and 5 m × 3 m.

7. Conclusions and Perspectives

This paper studied the thermo-hydro-mechanical (THM) responses of a case study of a high-level radioactive waste (HLW) repository based on the French concept within the framework of DECOVALEX-2019 project (Task E). Five teams were involved in this Task. Thermo-poro-elastic formulations were adopted. All teams proposed a 3D representation of the HLW repository with different levels of simplifications and different assumptions of boundary conditions. THM indicators for the design of the HLW repository (temperature and effective stress) and the pore pressure at two points at the repository level were analyzed along with the surface uplift. Numerical comparison between teams allowed to quantify the impact of assumptions and simplifications used for representing the HLW repository. Plane strain conditions were also assessed with respect to 3D modelling. Additional studies included mono and multi parametric sensitivity analyses, uncertainty and spatial variability analyses. Based on the modelling teams' results, best practice recommendations for modelling at the repository scale were drawn. Moreover, significant observations regarding the THM behavior of the considered HLW repository can be also made:

- At the mid-distance between two HLW cells, which is expected to have the highest effective stress, no tensile stress was found
- An importance ranking of all THM parameter was presented for the temperature, pore pressure and Terzaghi effective stress in which the most important parameters were permeability, Young's modulus and thermal conductivity;
- Uncertainty of THM parameters of surrounding layers does not influence significantly the THM behavior of the HLW repository at the selected observation locations;
- The maximum Terzaghi effective stress at the mid-distance between two cells shows low sensitivity to the drainage condition of the access galleries; and
- The numerical results of the spatial variability analysis show a negligible influence on the mean of maximum vertical Terzaghi effective stress with respect to the one obtained with the mean THM parameters as well as for the three different the spatial correlation lengths that were tested: 20 m × 12 m, 10 m × 6 m and 5 m × 3 m.

Acknowledgments

DECOVALEX is an international research project comprising participants from industry, government and academia, focusing on development of understanding, models and codes in complex coupled problems in sub-surface geological and engineering applications; DECOVALEX-2019 is the current phase of the project. The authors appreciate and thank the DECOVALEX-2019 Funding Organizations Andra, BGR/UFZ, CNSC, US DOE, ENSI, JAEA, IRSN, KAERI, NWMO, RWM, SÚRAO, SSM and Taipower for their financial and technical support of the work described in this report. The statements made in the report are, however, solely those of the authors and do not necessarily reflect those of the Funding Organizations.

Funding for LBNL's modeling work was provided by the Spent Fuel and Waste Science and Technology, Office of Nuclear Energy, of the U.S. Department of Energy under Contract Number DE-AC02-05CH11231 with Lawrence Berkeley National Laboratory.

Funding for Quintessa's modeling work was provided by Radioactive Waste Management Ltd.

UFZ/BGR teams work was supported by funding from the Federal Institute for Geosciences and Natural Resources (grant number 204-10088620) and within the iCROSS project (Integrity of nuclear waste repository systems – Cross-scale system understanding and analysis) funded by the Federal Ministry for Education and Research (BMBF) and the Helmholtz Association (grant numbers 02NUK053E, SO-093).

The various funding for conducting research work for DECOVALEX-2019 Task E is greatly acknowledged.

References

1. Delay J., Vinsot A., Krieguer J.M., Rebours H. and Armand G. 2007. Making of the underground scientific experimental programme at the Meuse/Haute-Marne underground research laboratory, northeastern France. Physics and Chemistry of the Earth, 32 (1/7): 2–18.

2. Armand G., Dewonck S., Bosgiraud J.M. and Richard-Panot L. 2015. Development and new research program in the Meuse Haute-Marne Underground Research Laboratory (France). 13th ISRM International Congress of Rock Mechanics. Montreal

3. Armand G., Bumbieler F., Conil N., de la Vaissière R., Bosgiraud J.M. and Vu M.N. 2017. Main outcomes from in situ thermo-hydro-mechanical experiments programme to demonstrate feasibility of radioactive high-level waste disposal in the Callovo-Oxfordian claystone. Journal of Rock Mechanics and Geotechnical Engineering, V.9, Issue 3, 415-427.

4. Mari J.L. and Yven B. 2014. 3D high resolution seismic model with depth: A relevant guide for Andra deep geological repository project. Marine and Petroleum Geology. 53, 133-153.

5. Conil N., Talandier J., Djizanne H., de la Vaissière R., Righini-Waz C., Auvray C., Morlot C. and Armand G. 2018. How rock samples can be representative of in situ condition: A case study of Callovo-Oxfordian claystones. Journal of Rock Mechanics and Geotechnical Engineering 10, 613–623. https://doi.org/10.1016/j.jrmge.2018.02.004

6. Yven B., Sammartino S., Geraud Y., Homand F. and Villieras F. 2007. Mineralogy, texture and porosity of Callovo-Oxfordian argillites of the Meuse/Haute-Marne region (eastern Paris Basin). Mémoires de la Société géologique de France.178: 73e90 (in French).

7. Robinet J.C., Sardini P., Siitari-Kauppi M., Prêt D. and Yven B. 2015. Upscaling the porosity of the Callovo-Oxfordian mudstone from the pore scale to the formation scale; insights from the 3H-PMMA autoradiography technique and SEM BSE imaging. Sedimentary Geology;321:1-10.

8. Song Y., Davy C., Troadec D., Blanchenet A.M., Skoczylas F., Talandier J. and Robinet J.C. 2015. Multi-scale pore structure of COx claystone: Towards the prediction of fluid transport. Marine and Petroleum Geology 65, 63-82.

9. de La Vaissière R., Armand G. and Talandier J. 2015. Gas and water flow in an excavation-induced fracture network around an underground drift: A case study for a radioactive waste repository in clay rock, Journal of Hydrology 521, p. 141–156

10. Giot, R., Auvray, C., Conil, N. and de La Vaissière, R. 2018. Multi-stage water permeability measurements on claystone by steady and transient flow methods. Engineering Geology 247, pp. 27–37

11. Robinet J.C., Sardini P., Coelho D., Parneix J., Pret D., Sammartino S., Boller E. and Altmann S. 2012. Effects of mineral distribution at mesoscopic scale on solute diffusion in a clayrich rock: example of the Callovo-Oxfordian mudstone (Bure, France). Water Resources Research, 48, (5):W05554.

12. Seyedi D., Armand G., Conil N., Vitel M. and Vu M.N. 2017. On the Thermo-Hydro-Mechanical Pressurization in Callovo-Oxfordian Claystone under Thermal Loading. Poromechanics VI: 754-761

13. Seyedi D., Vitel M., Vu M.N. and Armand G. 2018. Key parameters controlling thermo-hydro-mechanical pressurization in Callovo-Oxfordian claystone. International Symposium on Energy Geotechnics (SEG-2018). Lausanne, Switzerland

14. Vu M.N., Seyedi D. and Armand G. 2015. Thermo-poro-mechanical coupled processes during thermal pressurization around Nuclear Waste Repository. 6th Coupled Problems in Science and Engineering, May 18-20. Venice, Italy.

15. Vu M.N., Armand G. and Plúa C. 2019. Thermal Pressurization Coefficient of Anisotropic Elastic Porous Media. Rock Mech Rock Eng. https://doi.org/10.1007/s00603-019-02021-1

16. Bumbieler F., Plúa C., Tourchi S., Vu M.N. Vaunat J., Gens A. and Armand G. 2020. Feasibility of constructing a full-scale radioactive high-level waste disposal cell and characterization of its thermo-hydro-mechanical behavior. Submitted to Int. J. Rock Mech. Min. Sci.

17. Mohajerani M., Delage P., Sulem J., Monfared M., Tang A.M. and Gatmiri B. 2012. A laboratory investigation of thermally induced pore pressure in the Callovo-Oxfordian claystone. International Journal of Rock Mechanics and Mining Sciences. 52:112-121.

18. Braun P., Ghabezloo S., Delage P., Sulem J. and Conil N. 2018. Theoretical Analysis of Pore Pressure Diffusion in Some Basic Rock Mechanics Experiments. Rock Mechanics and Rock Engineering 51.5, pp. 1361–1378

19. Conil N., Armand G., Garitte B., Jobmann M., Jellouli M., Fillipi M., de la Vaissière R. and Morel J. 2012. In situ heating test in Callovo-Oxfordian claystone: measurement and interpretation. Proceeding of 5th Int. Conf. on Clays in natural and engineered barriers for radioactive waste confinement. Montpellier.

20. Conil N., Manon V., Plúa C., Vu M.N., Seyedi D. and Armand G. 2020. In Situ Investigation of the THM Behavior of the Callovo-Oxfordian Claystone. Rock Mechanics and Rock Engineering. https://doi.org/10.1007/s00603-020-02073-8.

21. Morel J., Bumbieler F., Conil N. and G. Armand. 2013. Feasibility and behavior of a full scale disposal cell in a deep clay layer. EUROCK 2013. Wroclaw.

22. Tourchi S., Vaunat J., Gens A., Vu M.N., Bumbieler F. 2019. Thermo-Hydro-Mechanical simulation of a full-scale steel-lined micro-tunnel excavated in the Callovo-Oxfordian Argillite. XIV International Conference on Computational Plasticity. Fundamentals and Applications (COMPLAS 2019), Barcelona, Spain

23. Plúa C., Manon V., Seyedi D. Armand G., Rutqvist J., Birkholzer J., Xu H., Guo R., Tatcher K.E., Bond A.E., Wang W., Nagel T., Shao H. and Kolditz O. 2020. Decovalex-2019: Task E final report. LBNL-2001265.

24. Seyedi D., Plúa C., Vitel M., Armand G., Rutqvist J., Birkholzer J., Xu H., Guo R., Tatcher K.E., Bond A.E., Wang W., Nagel T., Shao H. and Kolditz O. 2020. Upscaling THM modelling from small-scale to full-scale in-situ experiments in the Callovo-Oxfordian claystone. Submitted to Int. J. Rock Mech. Min. Sci.

25. COMSOL Multiphysics®. www.comsol.com. COMSOL AB, Stockholm, Sweden.

26. code_aster, 2016. https://code-aster.org/

27. Rutqvist J., Wu Y.-S., Tsang C.-F. and Bodvarsson G. A modeling approach for analysis of coupled multiphase fluid flow, heat transfer and deformation in fractured porous rock. International Journal of Rock Mechanics & Mining Sciences. 2002; 39, 429-442.

28. Rutqvist J. An overview of TOUGH-based geomechanics models. Computers & Geosciences. 2017; 108, 56–63.

29. Maul P. QPAC: Quintessa's general purpose modelling software. Quintessa Report QRS-QPAC-11; 2013. www.quintessa.org

30. Wang W., Kolditz O. Object-oriented finite element analysis of thermo-hydro-mechanical (THM) problems in porous media. Int. J. Numer. Methods Eng. 2007; 69 (1), 162 – 201

31. Kolditz O., Bauer S., Bilke L., Böttcher N., Delfs J.O., Fischer T., Görke U.J., Kalbacher T., Kosakowski G., McDermott C.I., Park C.H., Radu F., Rink K., Shao H., Shao H.B., Sun F., Sun Y.Y., Singh A.K., Taron J., Walther M., Wang W., Watanabe N., Wu Y., Xie M., Xu W., Zehner B. OpenGeoSys: an open-source initiative for numerical simulation of thermo-hydro-mechanical/chemical (THM/C) processes in porous media. Environ. Earth Sci. 2012; 67 (2), 589 – 599

32. Bilke, L., Flemisch, B., Kalbacher, T., Kolditz, O., Helmig, R., & Nagel, T. (2019). Development of Open-Source Porous Media Simulators: Principles and Experiences. Transport in Porous Media, 130(1), 337–361. https://doi.org/10.1007/s11242-019-01310-1

33. Garitte B., Nguyen T.S., Barnichon J.D., Graupner B.J., Lee C., Maekawa K., Manepally C., Ofoegbu G., Dasgupta B., Fedors R., Pan P.Z., Feng X.T., Rutqvist J., Chen F., Birkholzer J., Wang Q., Kolditz O. and Shao H. 2017. Modelling the Mont Terri HE-D experiment for the Thermal–Hydraulic–Mechanical response of a bedded argillaceous formation to heating. Environ Earth Sci 76, 345. https://doi.org/10.1007/s12665-017-6662-1

34. Tamizdoust M.M. and Ghasemi-Fare O. 2020. A fully coupled thermo-poro-mechanical finite element analysis to predict the thermal pressurization and thermally induced pore fluid flow in soil media. Computers and Geotechnics 117, 103250. https://doi.org/10.1016/j.compgeo.2019.103250

35. Coussy O. 2004. Poromechanics. Wiley.

36. Guo R., Xu H., Plúa C. and Armand G. 2020. Prediction of the thermal-hydraulic-mechanical response of a geological repository at large scale and sensitivity analyses. Submitted to Int. J. Rock Mech. Min. Sci.

37. Plúa C., Vu M.N., Seyedi D.M. and Armand G. 2020. Effects of inherent spatial variability of rock properties on the thermo-hydro-mechanical responses of a high-level radioactive waste repository. Submitted to Int. J. Rock Mech. Min. Sci.

38. Herman J. and Usher W. 2017. SALib: An open-source Python library for Sensitivity Analysis, Journal of Open Source Software, 2(9), 97, doi:10.21105/joss.00097.

39. Sobol I.M. 1993. Sensitivity analysis for non-linear mathematical models. Mathematical Modelling and Computer Experiments 1,407–414.